Considerations regarding the drag of the LOMlogger, a laser-based dust logger, to be deployed in water-filled drill holes of the IceCube Upgrade

Bachelor's Thesis in Physics

Presented by
Kübra Tekbiyik
01.08.2024

Erlangen Centre for Astroparticle Physics
Friedrich-Alexander-Universität Erlangen-Nürnberg

Supervisor: Prof. Dr. Claudio Kopper

Abstract

The IceCube Neutrino Observatory, located at the geographic South Pole, is a Cherenkov detector designed to observe high-energy neutrinos. With the upcoming IceCube Upgrade and the future IceCube-Gen2 project, the observatory's capabilities will be significantly enhanced. An important component of the IceCube Upgrade is the LOMlogger, a laser-based dust logger designed to measure particulate content within the bulk ice. By analyzing the resulting profiles, variations in particulate concentration can be detected and a 3D model of the ice layers can be constructed. This thesis focuses on determining the drag of the baffles of the LOMlogger to ensure a successful deployment in water-filled drill holes. Therefore, experiments were conducted in a water tank—with and without a pipe—using a pulley system to create real-world deployment conditions. The results show a significant increase in the drag force when the baffle is in a confined pipe environment simulating the borehole. The drag of the baffle was determined to be approximately 51 N for a deployment speed of 0.3 m/s and approximately 13 N for a speed of 0.17 m/s.

Zusammenfassung

Das am geographischen Südpol gelegene IceCube Neutrino Observatory ist ein Cherenkov-Detektor, der darauf ausgelegt ist, hochenergetische Neutrinos zu beobachten. Mit dem bevorstehenden IceCube Upgrade und dem zukünftigen IceCube-Gen2-Projekt werden die Fähigkeiten des Detektors erheblich verbessert. Ein wichtiger Bestandteil des IceCube Upgrades ist der LOMlogger, ein laserbasierter Staublogger, der dazu dient, den Partikelgehalt im Eis zu messen. Durch die Analyse der resultierenden Profile können Variationen in der Partikelkonzentration festgestellt und ein 3D-Modell der Eisschichten erstellt werden. Diese Arbeit konzentriert sich darauf, den Strömungswiderstand der Bürsten des LOMloggers zu bestimmen, um eine problemlose Installation in den wassergefüllten Bohrlöchern zu gewährleisten. Dazu wurden Experimente in einem Wassertank – mit und ohne Rohr – durchgeführt, wobei ein Flaschenzugsystem entwickelt wurde, um reale Einsatzbedingungen zu simulieren. Die Ergebnisse zeigen einen signifikanten Anstieg der Strömungswiderstandskraft, wenn sich die Bürsten in einem engen Rohr befinden, die das Bohrloch simuliert. Der Strömungswiderstand der Bürsten wurde auf etwa 51 N bei einer Einsatzgeschwindigkeit von 0,3 m/s und etwa 13 N bei einer Geschwindigkeit von 0,17 m/s bestimmt.

Contents

1 Introduction

> *"I have done a terrible thing, I have postulated a particle that cannot be detected."*
>
> by *Wolfgang Pauli* about the neutrino

Neutrinos dominate the universe as the most abundant massive elementary particle [1]. Since their postulation in 1930 by Wolfgang Pauli, in order to resolve the puzzle regarding the missing energy in beta decay and their experimental discovery later in 1956 by Cowan and Reines, these particles have fascinated scientists with their unique properties [2, 3]. In the standard model, neutrinos are fermions with a spin of one-half, belonging to the family of leptons, which includes three different flavors: electron-neutrino (ν_e), muon-neutrino (ν_μ) and tau-neutrino (ν_τ). The transformation of one flavour to another is described by the phenomenon of neutrino oscillation. Neutrinos, being almost massless, interact only via the weak force due to them being electrically neutral and not having a color charge [1]. This property makes them very difficult to detect, even though approximately 100 trillion neutrinos pass through a human body every second [4]. However, their weak interaction with matter also makes them perfect candidates for multi-messenger astronomy, providing accurate insights into their sources that are otherwise inaccessible [5]. A large volume is necessary to be able to detect neutrino interactions with matter, therefore using natural resources such as water or ice as the detector medium is reasonable. In 1991, a single test line of detection devices from AMANDA (Antarctic Muon And Neutrino Detector Array) at the South Pole proved the practicality of an in-ice neutrino telescope [6]. The follow-up experiment IceCube has been operating since 2011 and has made several major discoveries. In 2023, the IceCube Collaboration detected neutrino emission from the galactic plane at a significance level of 4.5σ [7]. These groundbreaking discoveries motivate the further development of the observatory. The IceCube Upgrade aims to increase the sensitivity of the detector by installing a few hundred additional optical sensors and new instrumentation [8]. One of the new components of the Upgrade is the laser-based LOMlogger - a new design of the dust logger - which consists of an emitter and a receiver module and baffles. It is designed to measure the particulate content of the ice. By evaluating the resulting layer profiles, the ice tilt can be mapped which is crucial for accurate event reconstructions [9]. To prevent complications during the installation session, the weight attached at the bottom of the string must be correctly determined [10]. This requires a thorough analysis of the LOMloggers drag, which is the focus of this thesis.

2 Neutrino Astronomy

The field of neutrino astronomy is young but rapidly evolving. Neutrinos are particularly suitable for identifying the sources of Cosmic Rays (CRs), making them perfect in this area of study. This chapter highlights the advantages of neutrinos over other messenger particles and discusses the sources of high-energy neutrinos. The final sections focus on their primary interactions with matter and the Cherenkov effect used for their detection, which is utilized by IceCube.

2.1 Role of Neutrinos in Multi-Messenger Astronomy

When thinking about astronomy, most people immediately think of large 'classical' telescopes that capture photons. However, photons are only one of many other messenger particles that can be used to observe the universe.

Although we can observe the sky in different wavelengths, such as radio or x-ray, observations with photons have the problem that they are quickly absorbed at higher energies by the Interstellar Medium (ISM) or interact with photon fields and therefore do not reach the Earth [5].

Instead, cosmic rays, which are charged atomic nuclei, can be used as messengers. Particularly, the sources of ultra-high-energy cosmic rays are of interest, as we currently have no explanation for how they are accelerated to such high energies. The energy spectrum and the flux of cosmic rays are both described by a power law. The flux decreases rapidly as the energy increases, which is why large detector areas are needed to detect high-energy cosmic rays. Another problem with CRs is that they get deflected by magnetic fields since they are charged, making it difficult to identify their sources, although detecting them is relatively easy [11].

Using neutrinos as messenger particles avoids this problem. When CRs interact with matter, they produce neutrinos, among other secondary particles, through the process:

$$p + N \rightarrow \pi^{\pm}, \pi^{0}, K^{\pm}, K^{0}, p, n, \ldots \tag{1}$$

For specific pion decays:

$$\begin{aligned} \pi^{+} &\rightarrow \mu^{+} + \nu_{\mu} \\ \pi^{-} &\rightarrow \mu^{-} + \bar{\nu}_{\mu} \end{aligned} \tag{2}$$

Since neutrinos are chargeless, their trajectories in space are straight. This allows astrophysical objects, possible origins of cosmic rays, to be directly associated with their detection. However, it should be mentioned that neutrinos interact only weakly and therefore very large detector areas are also necessary to detect them [11].

2.2 High-Energy Cosmic Ray and Neutrino Sources

High-energy CRs and neutrinos are believed to originate from both galactic and extragalactic sources [12].

The main candidates of CRs in the galactic spectrum are Supernova Remnants (SNRs), structures left behind after a star explodes. During these massive explosions, particles gain energy by repeatedly bouncing off the resulting shock front. Other candidates include pulsars, which can accelerate particles through their strong magnetic fields and binary systems that contain either a massive neutron star or a black hole [12].

Extra-galactic candidates primarily include Active Galactic Nuclei (AGN) and the associated blazars, which form a subclass of AGN. The core of these galaxies contains a supermassive black hole that, through mass accretion, generates highly energetic jets in which particles are accelerated. Gamma Ray Bursts (GRBs) are the most energetic explosions in the universe. Particle acceleration occurs again at the shock fronts during these events. Starburst galaxies, on the other hand, eject powerful winds during periods of intense star formation [12].

2.3 Detection of Neutrinos using the Cherenkov Method

As stated in section 1, neutrinos only interact via the weak force. Consequently, the cross-section for a neutrino interacting with matter is very small, making detection challenging. Large volume detectors are necessary to detect enough neutrinos to make statistically significant statements [6].

At high energies, deep-inelastic neutrino-nucleon (ν-N) scattering is the most common type of interaction. This interaction can occur in two ways: Charged Current (CC) interactions

$$\nu_l + N \rightarrow l + X, \tag{3}$$

and Neutral Current (NC) interactions

$$\nu_l + N \rightarrow \nu_l + X. \tag{4}$$

Both interactions produce a hadronic shower (X), but the CC channel also generates a charged lepton ($l = e, \nu, \tau$).

Cherenkov detectors, like the IceCube Observatory, observe light created by the charged particles, such as electrons or muons, resulting from these interactions [13]. When these charged particles move through a medium with a reflective index n at a velocity greater than the speed of light in that medium $\frac{c_0}{n}$, they emit radiation. Due to the particle's greater velocity, the wavefronts of the dipole radiation interfere constructively, producing the characteristic light cone. This is known as the Cherenkov effect. The resulting opening angle θ of the cone is determined by

$$cos(\theta) = \frac{1}{\beta n} \tag{5}$$

where β is the ratio of the particles's velocity to the speed of light in vacuum [14].

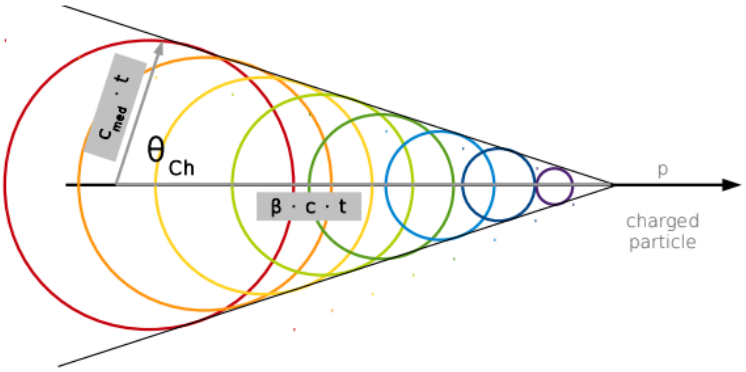

Figure 1: Illustration of the Cherenkov effect, showing the characteristic light cone produced when a charged particle moves through a medium faster than the speed of light in that medium [14].

The different event signatures caused by these neutrino interactions will be discussed in section 3.2.

3 IceCube Neutrino Observatory

The IceCube Neutrino Observatory is designed to detect high-energy neutrinos from astrophysical sources. The following chapter provides an overview of its architecture, main components and event signatures. Later in this section, the relevant properties of ice and the IceCube extensions will be discussed.

3.1 Structure and Components

The IceCube detector covers a total volume of one cubic-kilometer and is buried up to 2,450 meters deep in the Antarctic ice at the South Pole. Currently, three different arrays are used in IceCube. The primary in-ice array and its subarray, DeepCore, are used to detect neutrinos from different sources and energies. Additionally, the IceTop array, which surrounds the IceCube Laboratory (ICL) on the surface of the ice, is used for detecting cosmic ray air showers [10].

Equipped with 5,160 light sensors called Digital Optical Modules (DOMs), the in-ice array is deployed in the ice cap at depths ranging from 1,450 to 2,450 meters. The DOMs are distributed over 86 strings, following a hexagonal grid with a horizontal spacing of 125 meters. The primary in-ice array is designed to observe neutrinos within an energy range of TeV to PeV. Eight additional strings form the DeepCore subarray, which has a more compact arrangement of detectors. This allows the detection of particles with lower energies of 10-100 GeV [10].

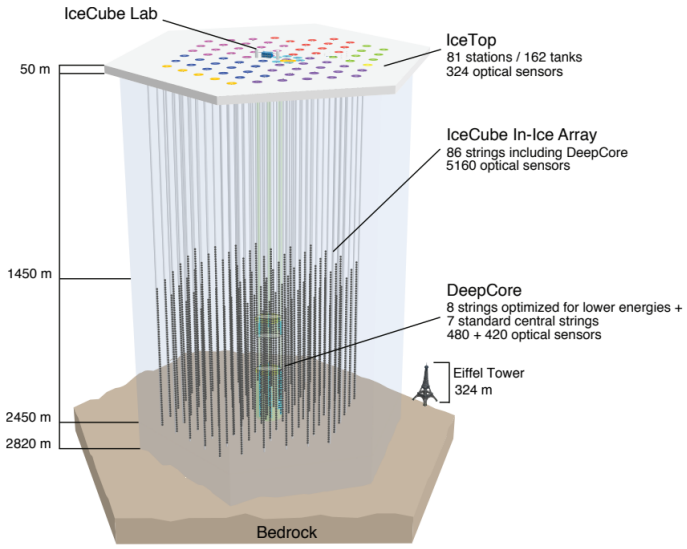

Figure 2: Schematic overview of IceCube's structure [10].

The centerpiece of a DOM is the 25 cm diameter Photo Multiplier Tube (PMT), which detects the Cherenkov light induced by neutrino interactions in the ice. Installed in a spherical 33 cm glass housing, the light sensors can endure the pressure when deployed

in the ice cap. The DOM is designed in such a way that it can record and process data almost completely independently and send it to surface computers of the ICL [10].

3.2 Signal Detection and Event Signatures

The interaction channel of a neutrino with the ice determines the detector signature. As already described in more detail in section 2.3, the resulting particles are charged and emit Cherenkov light that can be observed by the DOMs. Generally, the energy and direction determined from the events then provide information about the original neutrino [13].

Cascades are spherical showers of light (see Figure 3a). NC interactions of all neutrino flavours, where the neutrino transfers some energy onto the nucleon, cause a hadronic cascade. Furthermore, a CC interaction of a ν_e creates an electron that then initiates an electromagnetic cascade. A ν_τ CC interaction causes an event signature called the 'double-bang'. The first cascade occurs when the τ lepton is created and the second one when the τ decays [13].

Tracks are linear paths that are observed when a CC interaction occurs and a charged lepton is created. The charged lepton travels through the ice and leaves a trail of Cherenkov light (see Figure 3b). Tracks are mostly caused by ν_μ interactions, where the corresponding μ lepton travels relatively long distances through the medium, causing the typical signature [13].

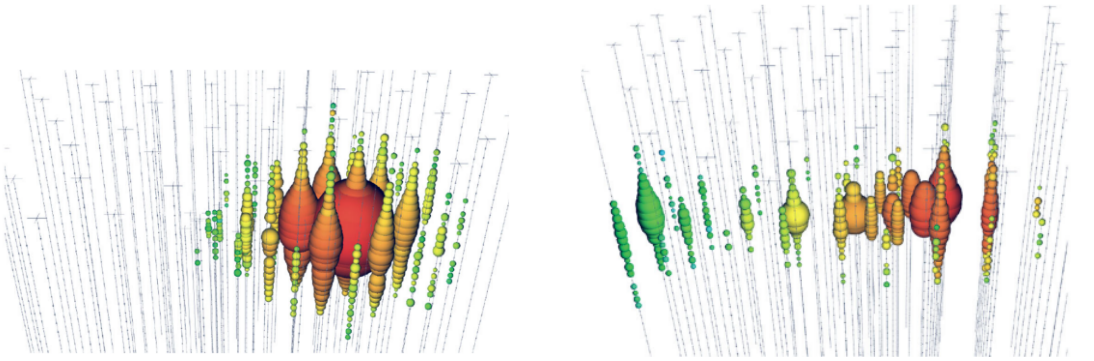

(a) Cascade event with the complete energy being contained within the detector volume .

(b) Track event of a muon escaping the detector with some remaining energy.

Figure 3: Each colored dot represents a hit DOM, with size indicating light amount and color indicating timing: red for early hits, blue for later hits [15].

3.3 Ice Properties

Since IceCube uses a natural Cherenkov medium, there is no opportunity to influence its optical properties. At depths where the IceCube array operates, the optical properties of the ice are determined by scattering and absorption by impurities [16]. Correct event reconstructions can only be achieved by in-situ calibration of the ice with special

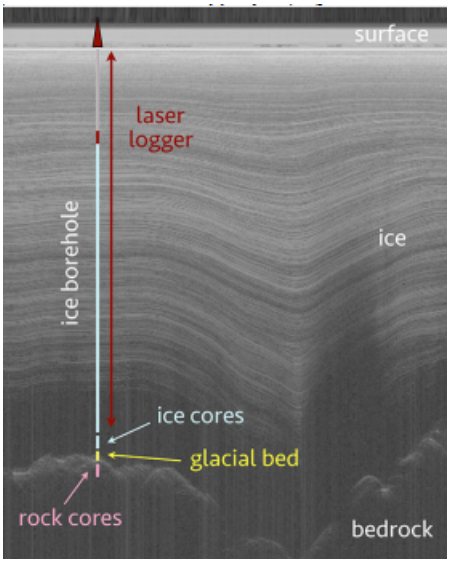

Figure 4: Layered structure of the ice revealed by a radargram. The deeper layers follow the shape of the bedrock beneath [18].

methods and devices.

Each year, a new layer of snow falls on the Antarctic ground. The snow then compresses over many years and forms distinct ice layers [17]. The precipitation itself contains impurities such as mineral dust or ash from volcanic activity, which means that each layer has a slightly different impurity concentration [16]. A stratigraphy of the entire bulk ice can be recorded using radar waves, revealing the layered structure (see Figure 4). Ice layers that formed at the same time are called isochrons [19]. The deviations of the isochrons from a horizontal line reflect the ice undulations, the so called ice tilt, caused by the topology of the underlying bedrock. In IceCube the tilt is parameterized using a device called dust logger [9]. How this works will be explained in more detail later in section 4. Photons created in neutrino interactions are primarily influenced by absorption and scattering. Effects such as the ice layer tilting and the anisotropy affect these processes. While the ice layer tilting changes the amount of dust particles the photons encounter, the anisotropy causes the absorption and scattering coefficients to vary as a function of direction [20].

3.4 IceCube Upgrade and IceCube-Gen2

To further improve the existing detector, different extensions such as the IceCube Upgrade and the IceCube-Gen2 are planned. This section provides a brief overview of those projects.

For the IceCube Upgrade, seven new boreholes will be drilled and equipped with different instruments. The resulting array will improve the detection of low-energy neutrinos due to the smaller spacing of the new strings (see Figure 5). Furthermore, IceCube's data from the last decade will be recalibrated using the improved methods from the Upgrade. One of the goals of the Upgrade is research and development of instrumentation for

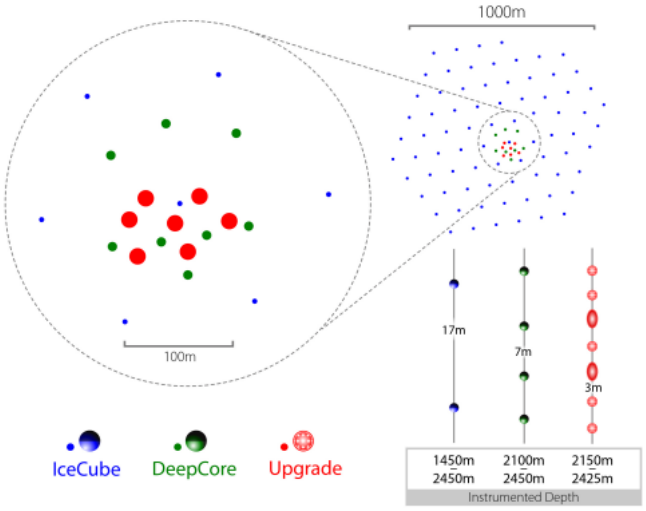

Figure 5: Layout of the IceCube Upgrade with seven new boreholes and their instrumentation spacing, enhancing the detection of low-energy neutrinos [8].

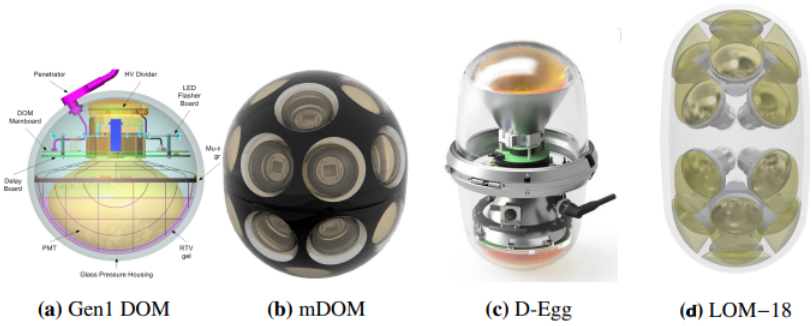

(a) Gen1 DOM **(b)** mDOM **(c)** D-Egg **(d)** LOM−18

Figure 6: Selection of different optical modules: (a) currently in use, (b) and (c) will be tested during the Upgrade and (d) proposed for Gen2. Modified from [21].

IceCube-Gen2, which is intended to cover a total volume of approximately 10 km^3 and be more sensitive to high-energy neutrinos [8]. The main sensors of the extensions are shown in Figure 6. IceCube's current in-ice array uses the already mentioned DOMs (a). For the Upgrade, the main operating photo detectors will be the mDOM (b) and D-Egg (c), which are more efficient in detection. The Long Optical Module (LOM) (d) is being studied and evaluated for IceCube-Gen2 [21]. Furthermore, the IceCube Upgrade will explore new depths, approximately 200 meters deeper than previously reached. Calibration instruments will be primarily installed in these regions to analyze the optical properties of these unknown ice layers [8]. The LOMlogger will play a key role in mapping the stratigraphy of these ice depths. The next section will discuss the functionality of the LOMlogger in detail.

4 The Laser-Based Dust Logger

The dust logger is a calibration instrument that measures the depth-dependent amount of particulates such as dust and volcanic ash. By analyzing the resulting profiles, variations in particulate concentration can be detected and a 3D model of the ice layers and their tilt can be constructed [9]. The following chapter describes the main working principle of a dust logger using the example of the previous model and explains the necessity of a new one. Furthermore, the new design will be described, along with potential problems that may arise during deployment.

4.1 Previous Model and Operational Principles

To understand the advancements in the new dust logger design, it is essential to first review the structure and functionality of the previous model. The approximately 1-meter-long dust logger, as shown Figure 7, mainly consists of three parts: the emitter at the top, the receiver at the bottom and brush baffles in between. The emitter utilizes a 404 nm diode laser, chosen specifically for its wavelength near the absorption minimum of glacial ice. The laser beam is shaped into a fan that covers a range of 60 degrees. The light is emitted horizontally into the ice surrounding the borehole. When the beam encounters bubbles or impurities in the ice, it is scattered and eventually absorbed. Only a very small fraction (10^{-10} to 10^{-6}) of the emitted photons are scattered in such a way that they reach the receiver (PMT) at the bottom. The approximately 46 cm diameter black nylon brush baffles ensure that the laser light passes through the ice around the borehole and does not reach the receiver directly through the borehole itself. This ensures that only the photons that have interacted with the ice layers are registered, allowing for an analysis of the optical properties of the bulk ice. Additionally, the baffles remove debris [9].

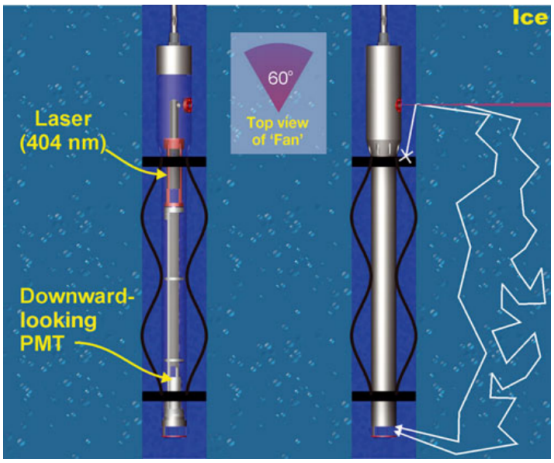

Figure 7: Schematic of the key components of the dust logger and its working principle. White lines represent the laser's scattering by bubbles or impurities. Black parts beneath the laser and above the PMT are the baffles that ensure the light travels through the ice [9].

The dust loggers were deployed in a total of eight boreholes. The positions are color-coded in the right picture of Figure 8. The first two instruments were attached to the bottom of the cable and were frozen into the ice together with the DOMs. The others were lowered into the borehole and then pulled back up before deploying the actual IceCube photo detectors. The stratigraphies recorded in these boreholes are shown in the left picture of Figure 8. These records provide the most detailed particulate stratigraphy available in Antarctica. By comparing the significant features in these profiles, the layer tilting can be mapped. The tilting noticeably increases the closer the layer is to the bedrock, since these layers more prominently follow the bedrock topography [9].

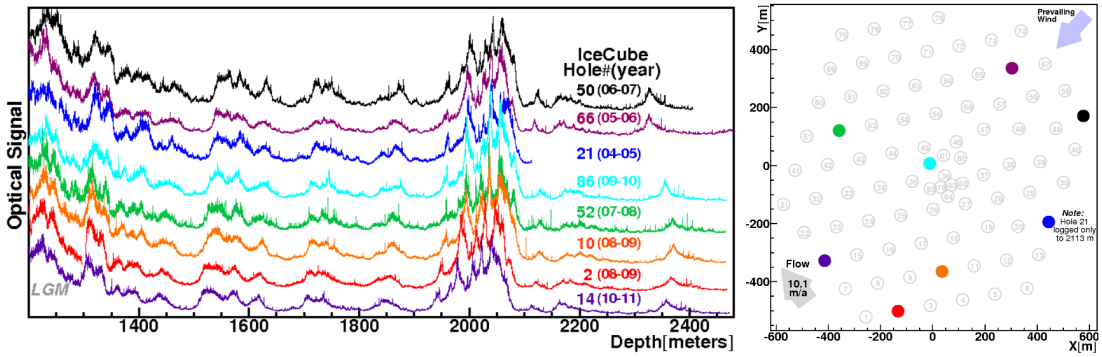

Figure 8: (**Left**) Optical signal profiles recorded in the boreholes, showing detailed particulate stratigraphy. By comparing significant features in these profiles, layer tilting can be modeled, with tilt variations becoming more pronounced closer to the bedrock. (**Right**) Locations of the boreholes where the dust loggers were deployed, indicated by color-coded markers [9].

4.2 Motivation for New Logging Instrumentation

As previously mentioned, the geometry of IceCube-Gen2 will extend beyond that of the current IceCube array. The horizontal string spacing is planned to be 240 meters, instead of the current 125 meters [22]. One problem that arises from this is that the ice layer tilt will be an even more significant factor. The greater the distance between the boreholes, the larger the deviations and consequently the greater the tilt [9]. If the tilt is not correctly modeled, it can significantly impact the event reconstructions. Therefore, logging of each hole will be necessary. Additionally, as already mentioned in section 3.4, new depths of approximately 200 meters deeper than previously reached will be explored. Deploying standalone dust loggers would be too expensive and time-consuming on this large scale. Hence, a new design is being developed that allows for logging with the instrumentation on the string. The new design will be evaluated during the IceCube Upgrade deployment in 2025/26 [23].

4.3 New Design and Functionality

The new design of the dust logger, referred to as the LOMlogger, will be accomplished by using and assembling already existing hardware. The receiver will be realized through a LOM, which has sixteen or eighteen 4-inch PMTs. It has a smaller diameter than

the Gen1 DOM but has an improved effective area [21]. The emitter will be realized through the Precision Optical Calibration Module (POCAM) (see Figure 9), which has an isotropic and homogeneous light emission. This device is ideal for use as the emitter of the LOMlogger, as it already has a multi-wavelength pulsed laser [24]. However, it needs to be modified to create a horizontal fan beam, similar to the original design. This can be achieved by removing the diffuser and using a collimator and a Powell lens.

Figure 9: The POCAM used in the IceCube Upgrade. The laser of the POCAM will be modified into a fan beam to serve as the LOMlogger emitter [24].

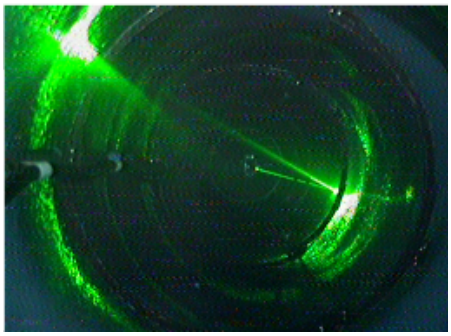

Figure 10: Camera footage showing light reflection at the water-ice transition in an IceCube borehole [23].

Main components such as the pressure housing, harness and steel cables will not be modified. Additionally, baffles will be added to stop reflections that can occur at the water-ice transition in the borehole (see Figure 10). The baffles have a diameter of 50 cm and currently consist of only one winding (see Figure 11). The emitter and the receiver instruments will be placed approximately 2 meters apart and the baffles are currently planned to be positioned exactly in the middle [23].

Figure 11: Picture of two baffle prototypes, each made from different materials (Polyamide 6 and Polyester).

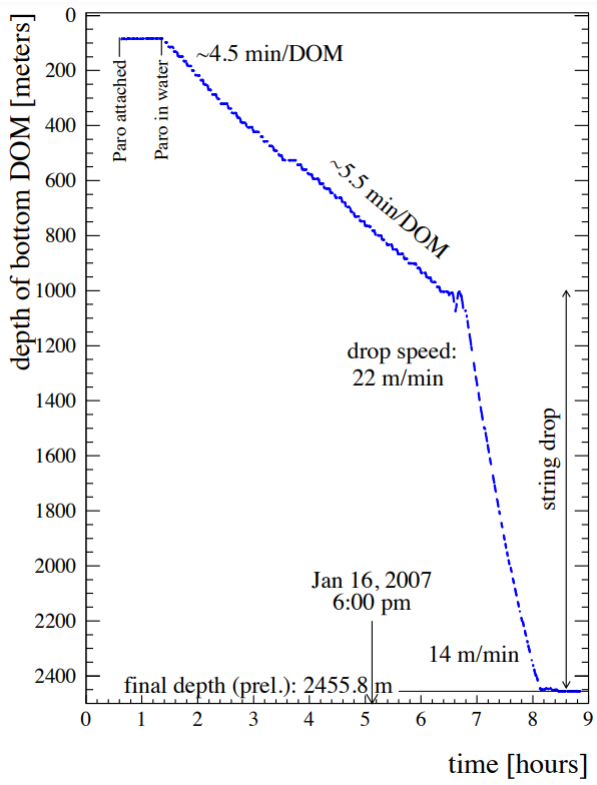

Figure 12: Deployment process of DOMs into the borehole. The graph shows the depth of the bottom DOM over time, indicating key phases, drop speeds and final depth [10].

Figure 13: CAD drawing of the LOMlogger with attachment cables. The LOM is shown at the top, the baffle in the middle and the POCAM at the bottom [25].

4.4 Deployment

Generally during deployment, weights are attached to the bottom DOM and secured to a steel cable, then lowered into the water-filled borehole created with the 5 MW Enhanced Hot Water Drill (EHWD). Subsequently, another DOM is attached and electrically connected, repeating this process until all remaining DOMs are in place. The remaining cable is then released into the borehole during the 'drop' phase [10]. To ensure the deployment proceeds smoothly and within a targeted window for every borehole, the lowering speeds need to be adjusted and controlled (see Figure 12). This requires recalculating the weight at the bottom shackle by determining and accounting for the drag caused by all devices, in particular the LOMlogger and its baffle (see Figure 13), which is the main focus of this thesis.

For the Upgrade, it is important to note that the deployment speed of approximately 0.37 m/s used previously will not be aimed for. Instead, a lower speed, likely between 0.15 m/s and 0.3 m/s, is being targeted [26].

Several potential issues could arise during the deployment of the LOMlogger. One problem that can occur is that the drag of the baffle is simply too large, causing the deployment to proceed very slowly. Another major concern is the risk of the brushes touching the wall of the borehole. If the string remains stationary for an extended period, such as 20 minutes, which can easily occur, the brushes may begin to freeze slightly into the wall. This can cause delays and complications in the overall process. The rate of ice-freeze-back is approximately 5-10 mm per hour, depending on the depth [23].

5 Fundamental Fluid Mechanics for Experimental Analysis

Understanding fluid mechanics and the forces acting on the LOMlogger and its baffle during deployment in the water-filled borehole is crucial for determining the device's drag and ensuring a successful deployment. This chapter provides an overview of the most important aspects of fluid mechanics relevant to the experiment, focusing on the concept of the Reynolds number, the buoyancy force and the definition of drag force and drag coefficient. Source [27] serves as the primary reference for the content of this chapter.

5.1 Reynolds Number

The Reynolds number is one of the key parameters in fluid mechanics. In many cases, it is more useful to label dimensionless quantities, such as the Reynolds number, as 'large' or 'small' in comparison to dimensional quantities like forces. The Reynolds number represents the ratio of inertial forces to viscous forces and is defined as:

$$\mathrm{Re} = \frac{\rho V L}{\mu} \tag{6}$$

where ρ is the density of the fluid, V the velocity, L the characteristic length of the object and μ the dynamic viscosity of the fluid. Since the characteristic length is not explicitly defined, it should always be clearly stated what is chosen for it.

The Reynolds number helps distinguish between different fluid dynamic regimes: for small Re the flow is laminar, meaning it flows smoothly, while for large Re the flow is turbulent. In the case of flow through a round pipe, it is observed that for $\mathrm{Re} < 2100$ the flow is laminar and for $\mathrm{Re} > 4000$ the flow is turbulent. In between these values, the flow can exhibit both behaviors. The Reynolds number also plays an important role in testing prototypes. To ensure that results obtained from a scale model can be accurately transferred to a prototype, the Reynolds numbers for both the prototype and the model must be the same.

5.2 Buoyancy

When an object is submerged in a fluid, it experiences an upward force called the buoyancy force F_b. If the buoyancy force is larger than the weight force of the object, the object floats on the surface, if it is smaller, the object sinks. According to Archimedes' principle, the buoyancy force can be expressed as:

$$F_b = \rho\, V g \tag{7}$$

where ρ is the fluid density, V the displaced volume of fluid and g the free-fall acceleration.

One method to determine the buoyancy force is by comparing the weight of the object in air with its weight when submerged in water. The difference between those two gives the buoyancy force directly. It is important to know the buoyancy of the baffles attached to the LOMlogger to later correctly determine the overall drag during deployment.

5.3 Drag Force and Drag Coefficient

The drag force F_d is a force caused by the motion of an object through a fluid and acts opposite to the direction of motion. The drag force is defined as:

$$F_d = \frac{1}{2}\rho v^2 C_d A \tag{8}$$

where ρ is the fluid density, v the velocity of the object relative to the fluid, C_d the drag coefficient and A a reference area of the object. As with the Reynolds number, the reference area A is not explicitly defined and therefore should always be specified. Usually A is chosen as the frontal area of the object. The drag coefficient C_d is a dimensionless number and is depended on several factors such as the shape of the object, the flow characteristics and the Reynolds number.

During the deployment in the IceCube Upgrade, it is necessary to account for the drag force of the dust logger and its baffles to ensure the descent speed into the borehole is within acceptable limits and proceeds smoothly.

5.4 Measurement Techniques and Numerical Simulations

In industry, it is common to use large air or water tunnels to observe various objects and how they behave under specific conditions. In many cases, prototype and model testing plays a crucial role in this process.

Another method of analyzing the forces acting upon a body is through numerical simulations such as Computational Fluid Dynamics (CFD). CFD simulations involve solving complex equations that describe how the fluid flows around an object. These simulations are a very useful tool for identifying potential issues with a specific design and the flow conditions, allowing engineers and scientists to make adjustments before the actual use or testing.

For this thesis, a CFD simulation using COMSOL Multiphysics was conducted with a CAD (Computer-Aided Design) model of the baffle. After failing to obtain consistent results for the drag force and consulting with professionals in fluid dynamics, it was concluded that simulating complex objects such as the baffle is nearly impossible. Only approximate results could be obtained by simulating the baffle as a type of porous material [28].

6 Drag Characterization of the LOMlogger Baffle

While simulations provide valuable insights, practical experiments are essential to accurately determine the drag force, as they capture real-world conditions and interactions. To determine the drag of the baffle, an experiment was designed and conducted in a water tank. The following chapter will describe the experimental setup, the methodology used and the results obtained from these tests.

6.1 Experimental Setup and Assembly

To replicate the deployment of the LOMlogger in a water-filled drill hole in a laboratory setting, a pulley system (see Figure 14a) was designed. This system was used to lower and raise the baffle in a water tank. Experiments were carried out with and without a pipe of 56 cm diameter, which was used to simulate a borehole and recreate real-life conditions during deployment.

The pulley system consists of two pulleys connected by a polypropylene rope. During the experiment, various weights or the baffle are attached to the ends of the rope and lowered into the water. Carabiners were used to securely attach the weights to the rope. To determine the drag of the baffle, it is essential to measure the acceleration of the experimental system. For this purpose, the pulleys are designed with spokes that function as an optical encoder. Using a TCRT5000 infrared sensor [29], whose functionality is explained in detail in section 6.2, and the parameters of the wheel, the speed of the pulley and the rope can be determined at any time. The pulley system was mounted on an existing crane support in the room where the water tank was located, with the mounts specifically designed and 3D printed to fit. The pulleys were secured with nuts and Loctite, while shaft collars were used to fix the axle. Clamps were used to correctly align the system and ensure the pulleys rotated as freely as possible. The axis of the pulleys, housed in deep groove ball bearings, allowed for smooth and efficient rotation.

Furthermore, an analysis of the mount friction indicated that the friction within the ball bearings remained predominantly constant under a specific bearing load, with an additional velocity-dependent term. However, a measurement concept was devised in which this friction does not need to be considered in the calculations. This is because only the difference between a reference measurement without the baffle and the measurement with the baffle is analyzed. This difference is solely due to the buoyancy force and the drag of the baffle, as the friction in the mounts is the same in both measurements and thus can be ignored.

6.2 TCRT5000 Infrared Sensor

6.2.1 Functionality and Programming

The TCRT5000 sensor (see Figure 15) continuously emits infrared light, and the phototransistor receives the reflected light, generating an electrical signal. This allows the detection of objects or surface changes. The returned signal is then processed by a

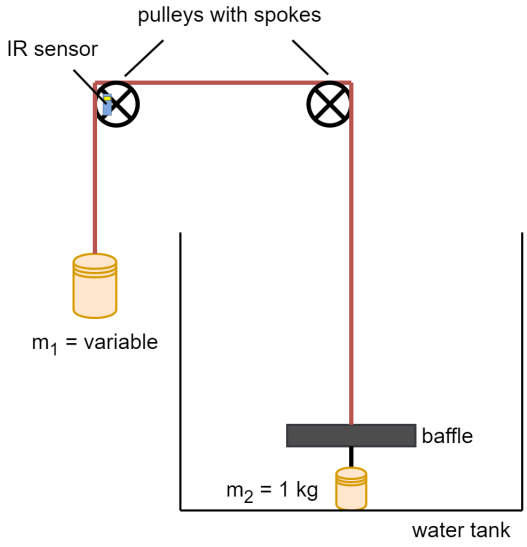

(a) Schematic of the experimental setup, showing the most important components.

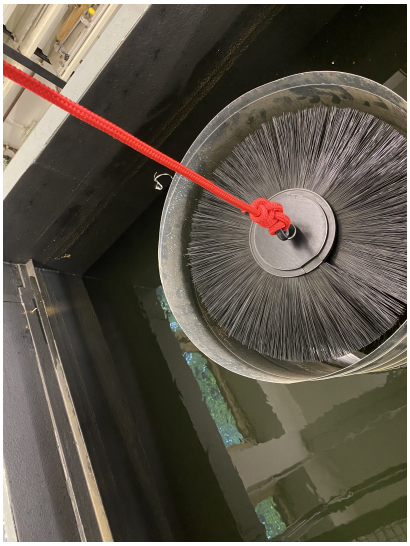

(b) Picture of the baffle being lowered into the pipe that simulates the borehole.

Figure 14: Experimental setup for measuring the effect of the baffle in different scenarios.

microcontroller, in this case, the Arduino Nano. Additionally, the sensitivity of the sensor can be adjusted using a potentiometer.

Using the Arduino Nano, the TCRT5000 was programmed to detect each transition at the spokes (each signal change) of the wheel and to output the corresponding timestamp. From these timestamps, the wheel circumference and the diameter of the rope, the distance traveled and thus the speed and acceleration can be calculated.

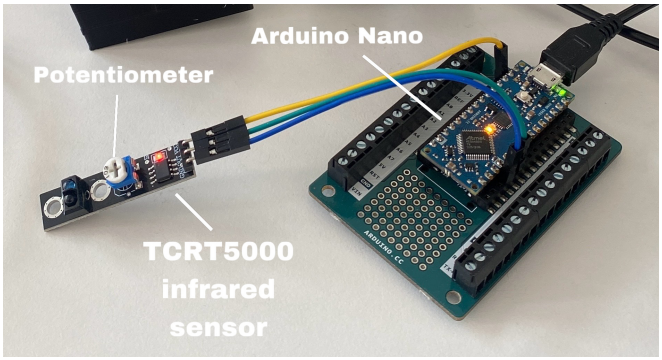

Figure 15: Connection of the TCRT5000 infrared sensor to the Arduino Nano.

The configured Arduino program has a time resolution of one millisecond. Additionally, a one millisecond delay was included to prevent potential issues with overly rapid electrical data processing.

6.2.2 Validation of Sensor Performance

To verify the accurate recording of measurement data and the subsequent calculation of the wheel's speed, the wheel and its axle were attached to a drill. The drill's Revolutions Per Minute (RPM) was known from the data sheet. The wheel was successfully tested at 500 RPM and 1750 RPM. The recorded and calculated RPM matched the expected values within the margin of measurement error.

6.2.3 Encountered Issues

3D printing results in objects having two different surface textures (see Figure 16). This can cause issues with the detection of transitions on the pulley. Both surfaces were tested with the TCRT5000. The results showed that the glossy side is better suited for measurements. When using the matte side, issues such as double measurement points frequently occurred. The problems with the matte side are likely due to diffuse reflection, where the light is scattered in many directions because of the uneven surface, making detection harder. In contrast, the glossy side reflects light in a single direction, providing a stronger and more focused signal. The same problem also arises if the sensor is not placed close enough to the wheel. In that case, the light-dark and dark-light transitions are not identified as equally long.

(a) Glossy surface of the pulley wheel.

(b) Matte surface of the pulley wheel.

Figure 16: Comparison of matte and glossy pulley wheel surfaces. Surface texture can influence sensor detection accuracy.

Another issue that arises is the presence of outlier data points, even when using the glossy side of the wheel (see Figure 17). It was found that these deviations always occur after one full rotation of the wheel. This suggests that a single transition at one spoke is being multiply detected. It was also observed that when summing the data points of the individual outlier groups, the result matches the actual measurement value. Since the cause of this systematic hardware error is known, it will be accounted for and corrected in the data analysis.

6.3 Determining the Buoyancy of the Baffle

Determining the buoyancy of the baffle is essential, as it affects the net force acting on the baffle in water. This is crucial for precise drag measurements and for ensuring a

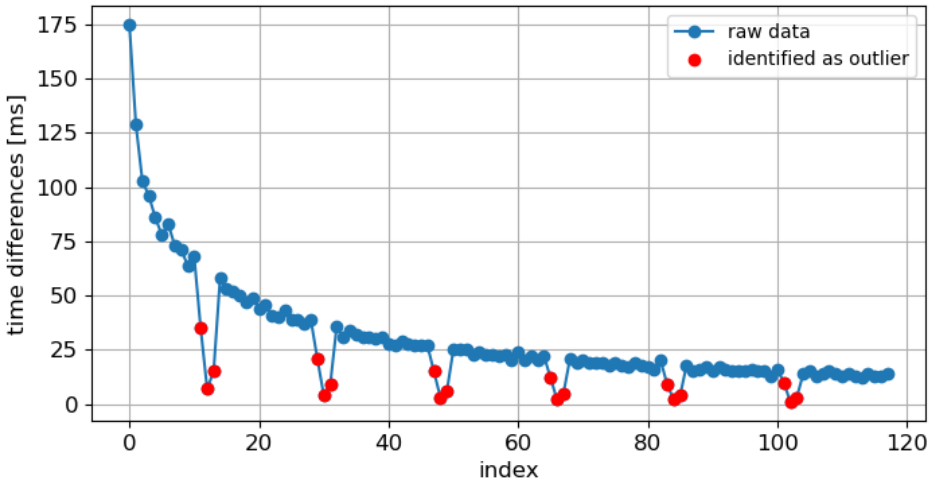

Figure 17: Exemplary plot of time differences between successive timestamps, which are recorded for each detected transition. The plot shows raw data and identified outliers marked in red. Outliers occur after each full wheel rotation, indicating issues with multiple detections of a single transition.

stable deployment.

To determine the buoyancy of the baffle, the method of measuring the weight difference in and out of the water was used. The baffle had to be completely submerged underwater. Since the buoyant force alone causes the baffle to float on the surface, a 0.5 kg weight was attached below the baffle with a carabiner. The measurement of the different weights was carried out using a spring scale. It is important to note that the additional weight below the baffle (0.5 kg + carabiner) also experiences buoyancy in the water. This must be measured and subtracted from the overall difference to obtain the buoyancy of the baffle alone, without the additional weight. The individual measurement results are shown in Table 1.

Table 1: Measurement results of different weights in air and in water.

Measurement	**Condition**	**Weight (N)**
Baffle without additional weight ($F_{\mathrm{B,\,air}}$)	In Air	11.3 N
Additional weight ($F_{\mathrm{W,\,air}}$)	In Air	6.1 N
Baffle with additional weight ($F_{\mathrm{B+W,\,air}}$)	In Air	17.4 N
Baffle with additional weight ($F_{\mathrm{B+W,\,water}}$)	Underwater	1.35 N
Additional weight ($F_{\mathrm{W,\,water}}$)	Underwater	4.4 N

From these measurements, the buoyant force for the additional weight is calculated as

follows:

$$\begin{aligned} F_{\text{b, W}} &= F_{\text{W, air}} - F_{\text{W, water}} \\ &= 6.1\,\text{N} - 4.4\,\text{N} \\ &= 1.7\,\text{N} \end{aligned} \tag{9}$$

To determine the buoyant force for the baffle itself, the buoyant force of the additional weight is subtracted from that of the baffle with the additional weight:

$$\begin{aligned} F_{\text{b, B}} &= F_{\text{B+W, air}} - F_{\text{B+W, water}} - F_{\text{b, W}} \\ &= 17.4\,\text{N} - 1.35\,\text{N} - 1.7\,\text{N} \\ &= 14.35\,\text{N} \end{aligned} \tag{10}$$

The net force on the baffle in water is calculated by subtracting the weight of the baffle in air from its buoyant force. This shows how much the baffle is lifted or pushed down in the water. In this case, the net force is:

$$\begin{aligned} F_{\text{net, B}} &= F_{\text{b, B}} - F_{\text{B, air}} \\ &= 14.35\,\text{N} - 11.3\,\text{N} \\ &= 3.05\,\text{N} \end{aligned} \tag{11}$$

Submerged in water, the baffle experiences a upward net force of 3.05 N.

6.4 Methodology

6.4.1 Data Collection

Several datasets were collected and analyzed to determine the drag on the baffle. A total of five different weights were used, responsible for the accelerating force in the system (weight m_1 in Figure 14a). For each weight, six datasets were recorded, with three measurements taken without the baffle (serving as reference measurements) and three measurements with the baffle. Additionally, two scenarios were investigated. The experiment was conducted both in an open water tank and with a pipe (d = 56 cm). The pipe's function is to simulate a borehole and recreate real-life conditions during deployment. The datasets are presented in Table 2.

Table 2: Comparison of weights used in different scenarios of the experiment. For each weight, six measurements were taken: three without baffle and three with baffle.

Open water tank without pipe	**With pipe (d = 56cm)**
2500g	2500g
3000g	3000g
3500g	3500g
4000g	4000g
4500g	4500g

In this work, the focus will be on the results of the extreme cases, specifically for the weights of 2500g and 4500g.

6.4.2 Data Processing and Analysis

The measurements always began with the weight below the baffle at the bottom of the water tank. This ensured that the maximum possible distance could be covered. This consistent starting condition was critical for maintaining the repeatability of the measurements. During the processing of raw data, outliers (see section 6.2.2) were first identified, summed and then reinserted in the correct position in the dataset. The corrected dataset is then used to calculate the distance traveled. A spline fit is then applied to this corrected distance and its derivatives are taken to obtain the speed and acceleration of the system. It is important to note that no error analysis was performed on the spline fit and that the error propagation increases with each subsequent derivative. Specific plots in the results section will highlight this consideration.

To determine the drag of the baffle from the existing datasets, the reference measurements need to be compared with the measurements taken with the baffle. The focus here is on the difference in speed-dependent accelerations, as the drag is dependent on velocity (see equation 8). Consequently, the difference reflects only the drag and buoyancy of the baffle. Since the friction in the mounts is the same for both measurements, it does not need to be considered further in the calculations.

6.5 Results

The following sections present the results of the experiments, comparing measurements in both an open water tank and a water tank with a pipe to simulate real deployment conditions. A complete analysis with the respective plots for the first example is carried out in both sections. For other measurements, only critical plots that require further explanation are presented. All other plots for every measurement can be found in Appendix A.

6.5.1 Open Water Tank without Pipe

The initial experiments were carried out without the baffle. This set of measurements serves as a reference to compare with the data obtained with the baffle installed.

Main accelerating weight: 2500g

The distance-time, velocity-time, acceleration-time and acceleration-velocity plots for the reference measurements are shown in Figure 18. The applied spline fit over the distance curve allows for the calculation of speed and acceleration profiles over time through differentiation. The spline fit is of degree 5 with a smoothing factor of 1, applied to reduce the effect of fluctuations in the data for a more accurate representation of the underlying trend. The data points in the distance plot represent the points after correcting the outliers from the timestamps (see section 6.2.3).

From the distance-time plot (see Figure 18a), a consistent increase in distance with time is observed. The curve shows a parabolic trend, indicating that the object is accelerating as it moves.

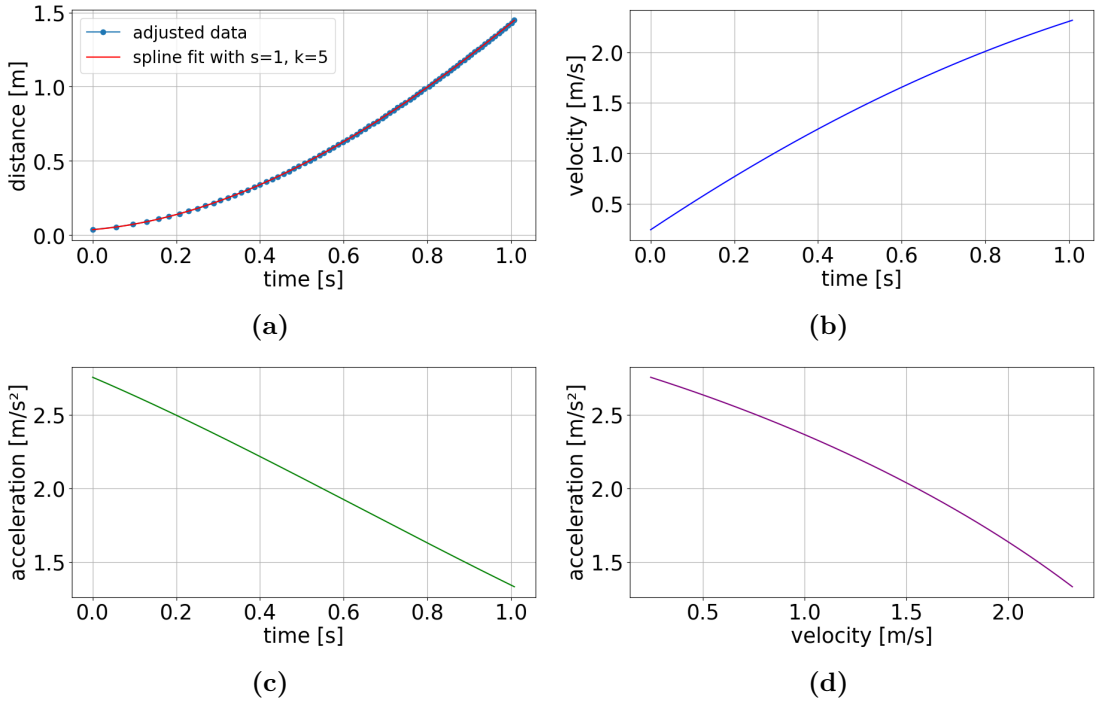

Figure 18: Reference measurements for the open water tank for the first 2500g measurement.

The velocity-time plot (see Figure 18b) reveals a non-linear increase in velocity over time. This suggests that the system does not experience constant but variable acceleration.

These findings are supported by the acceleration-time plot (see Figure 18c), which shows a almost linear decreasing trend. This behavior is likely due to the presence of two frictional components in the system: a dominant constant frictional term and a velocity-dependent term that increases with speed.

Finally, the acceleration-velocity plot (see Figure 18d) shows an inverse relationship between velocity and acceleration. As the velocity increases, the acceleration decreases.

The overall trend confirms that while the system is accelerating, the rate of acceleration decreases with time.

Next, the experiment was conducted with the baffle attached. The corresponding plots are presented in Figure 19.

The distance-time plot for the baffle measurement (see Figure 19a) shows a similar trend to the reference measurement but with a reduced acceleration. This is due to the presence of the additional drag force of the baffle.

The final velocity (see Figure 19b) is lower compared to the reference and the acceleration decreases non-linear with time, confirming the velocity-dependent resistance

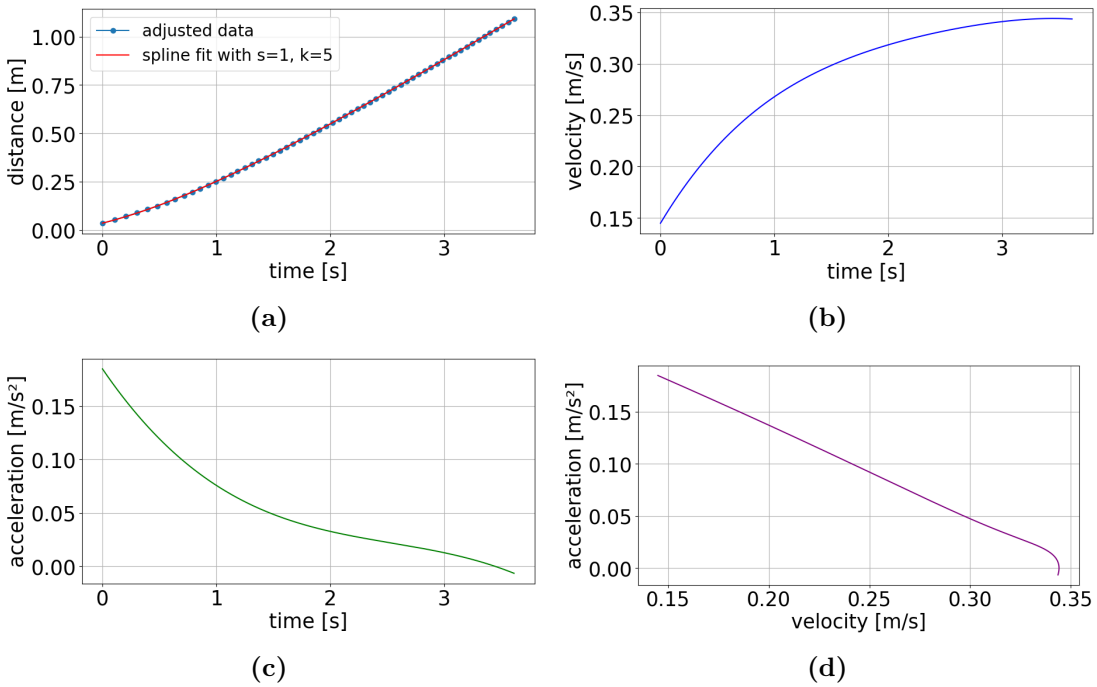

Figure 19: Measurements with the baffle for the open water tank for the first 2500g measurement.

caused by the baffle (see Figure 19c).

The acceleration-velocity plot (see Figure 19d) highlights the greater decrease in acceleration compared to the plot without the baffle. Again an inverse relationship between velocity and acceleration can be observed, but this effect is more pronounced in the measurement with the baffle. This is due to the drag force, which is proportional to the square of the velocity, causing the acceleration to decrease even more rapidly as the velocity increases. The quadratic relationship between drag and velocity holds because of the turbulent flow regime in which the baffle is operating.

Figure 20 shows the analysis of the acceleration difference between the reference measurement without the baffle and the measurement with the baffle. First, the velocity interval in which both accelerations were present was determined. Then, the acceleration values of with the baffle were subtracted from those of without the baffle. The acceleration difference increases with velocity, further confirming that the baffle introduces drag that grows with velocity. In summary, these plots clearly demonstrate the effect of the baffle on the system's dynamics.

To determine the force, the mean acceleration difference was taken and used with Newton's second law, $F = m_{tot} \cdot a$. Here, m_{tot} is the total mass of the accelerating system, including the two weights m_1 and m_2, the baffle, the rope weights and the carabiners. The mean acceleration difference was chosen because the difference is very small, as shown in the corresponding plot. Consequently, we approximate the acceleration difference to be about 2.68 m/s^2 at a speed of approximately 0.3 m/s. The

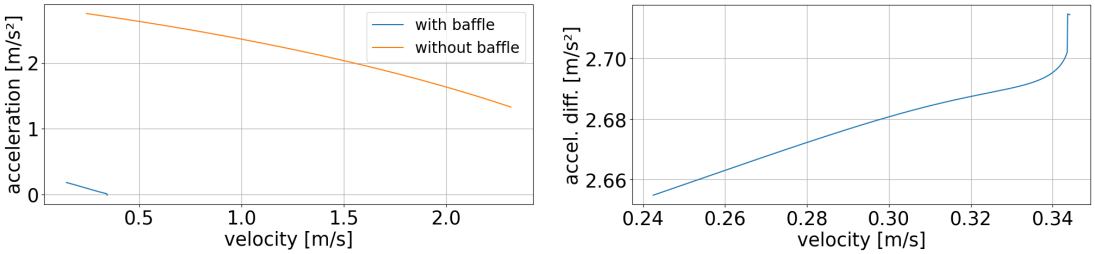

(a) (b)

Figure 20: Analysis of the acceleration difference for the first 2500g measurement without the pipe.

resulting force is then 14.063 N.

This calculated force includes both the buoyancy and the drag of the baffle. Since buoyancy is contributing to the acceleration of the system, it must be added to the resultant force to determine only the drag of the baffle.

The same analysis was performed for three different datasets. The results are presented in Table 3.

Table 3: Results of the three experiments conducted with a main accelerating weight of 2500g in the open water tank.

Experiment	Mean Acceleration Difference (m/s^2)	Resulting Force (N)
1	2.677	14.063
2	2.772	14.564
3	2.782	14.615

The mean drag force for the 2500g weight, based on the three measurements, is calculated to be 14.41 N with a sample standard deviation of 0.31 N. This result corresponds to a speed of 0.3 m/s.

Main accelerating weight: 4500g

The different plots for the reference measurement with the 4500g accelerating weight are shown in Figure 33.

The distance curve (see Figure 33a) shows a similar consistent increase in distance with time as with the 2500g weight. However, the curve shows a steeper slope, indicating a higher acceleration due to the increased mass.

The velocity-time plot (see Figure 21a/Figure 33b) reveals a more pronounced non-linear increase compared to the 2500g weight. This is likely due to issues in data processing, such as overfitting or underfitting of the spline to the data points. It is important to

note that no error analysis was performed on the spline fit, which means potential fitting inaccuracies in the data have not been accounted for.

The acceleration (see Figure 21b/Figure 33c) also shows a decreasing trend, similar to the 2500g weight, but with higher initial acceleration values, which is caused by the increased weight. Again, this behavior can be attributed to the presence of both constant and velocity-dependent frictional components. The wave-like pattern is presumably a result of the unaccounted error propagation of the spline fit.

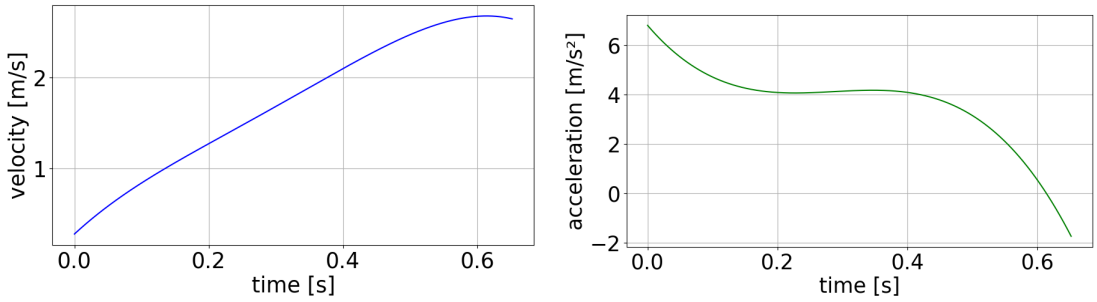

(a) **(b)**

Figure 21: The velocity-time (a) and acceleration-time (b) plots for 4500g without baffle illustrate potential error propagation issues in the spline fit, indicated by the non-linear increase in velocity and the wave-like pattern in the acceleration data.

The same issue also applies to the acceleration-velocity plot (see Figure 33d).

The observations made for the measurements with the baffle at 4500g (see Figure 34) are consistent with those seen in the comparison of the 2500g measurements with and without the baffle.

It is particularly evident that the final velocity is smaller than that of the reference measurement (see Figure 34b) and that the acceleration-velocity plot displays a steeper slope (see Figure 34d).

These findings again confirm the presence of the noticeable drag force introduced by the baffle.

The acceleration difference between the reference measurement and the measurement with the baffle is presented in Figure 22. Ideally, the graph in Figure 22b should show an increase in acceleration with velocity as already seen for the 2500g weight. However, this is not observed here due to the unaccounted error propagation. The error, causing the acceleration difference to appear to decrease with increasing velocity, originates from inaccuracies in the reference measurement. The force resulting from the mean acceleration difference is 43.931 N.

The results of all three measurements are presented in Table 4.

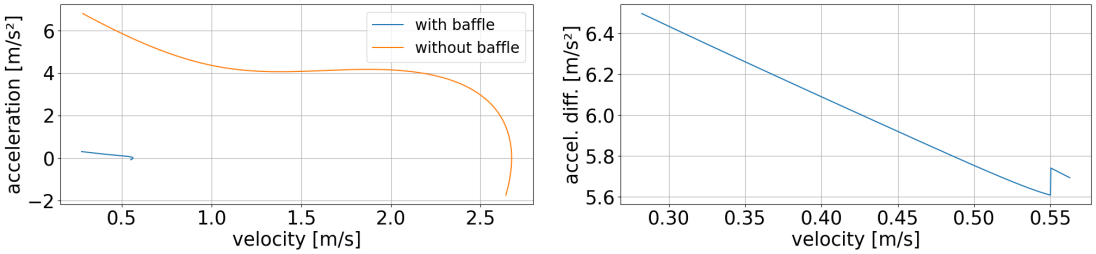

(a) **(b)**

Figure 22: Acceleration-velocity (a) and acceleration difference-velocity (b) plots for 4500g, illustrating potential error propagation in the spline fit. The right plot should ideally show an increasing trend with velocity.

Table 4: Results of the three experiments conducted with a main accelerating weight of 4500g in the open water tank.

Experiment	Mean Acceleration Difference (m/s^2)	Resulting Force (N)
1	6.024	43.691
2	5.801	42.078
3	5.272	38.239

The mean drag force for the 4500g weight, based on the three measurements, is calculated to be 41.34 N with a sample standard deviation of 2.80 N. This result corresponds to a speed of 0.45 m/s.

The observations from the open water tank provide a solid foundation. The significant influence of the baffle on the system's dynamics has been clearly demonstrated, with noticeable differences in velocity and acceleration profiles. This foundational understanding sets the stage for the next set of experiments, where the effects of the pipe on the system's behavior will be analyzed.

6.5.2 Water Tank with Pipe

To simulate a borehole during deployment, the following experiments were carried out in a water tank with an additional pipe.

Main accelerating weight: 2500g

The reference measurement without the baffle is similar to the one for the same weight without the pipe. The plots can be found in Figure 42.

The distance-time plot (see Figure 23a/Figure 43a) for the measurement with the baffle displays a different trend: the motion with the baffle attached is now linear, with a constant but lower velocity.

Examining the velocity plot (see Figure 23b/Figure 43b), it is also evident from the

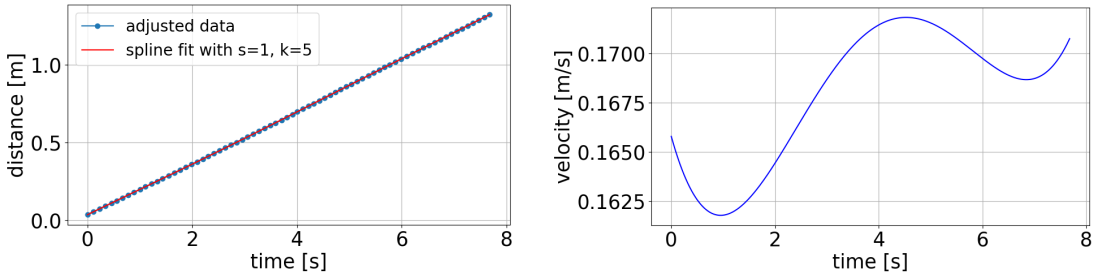

(a) (b)

Figure 23: Distance-time plot (a) in the pipe scenario showing linear motion with the baffle attached. Velocity-time plot (b) indicating a constant velocity of 0.167 m/s, implying zero acceleration.

scale that the velocity is indeed constant, which implies an acceleration of zero. The velocity remains constant at 0.167 m/s.

Since the acceleration is zero, the acceleration difference is simply that of the reference measurement without the baffle at the same speed. The resulting force of 14.940 N now corresponds to a velocity of 0.167 m/s.

The results of all three measurements are presented in Table 5.

Table 5: Results of the three experiments conducted with a main accelerating weight of 2500g in a simulated borehole scenario.

Experiment	Corresponding Velocity (m/s)	Resulting Force (N)
1	0.168	14.940
2	0.167	9.017
3	0.167	14.028

The mean drag force for the 2500g weight in a constraint environment, based on the three measurements, is calculated to be 12.66 N with a sample standard deviation of 3.19 N.

Main accelerating weight: 4500g

The reference measurement without the baffle is again essentially the same as the reference measurement from the experiment without the pipe. The corresponding plots are displayed in Figure 48.

With the baffle attached, the motion again becomes linear with a constant velocity of now approximately 0.3 m/s as seen in Figure 49.

The resulting force of 51.403 N corresponds to the velocity of 0.3 m/s, since the acceleration of the measurement with the baffle is zero.

The results of all three measurements are presented in Table 6.

Table 6: Results of the three experiments conducted with a main accelerating weight of 4500g in a simulated borehole scenario.

Experiment	**Corresponding Velocity (m/s)**	**Resulting Force (N)**
1	0.306	65.007
2	0.306	37.539
3	0.305	51.403

The mean drag force for the 4500g weight in a constraint environment, based on the three measurements, is calculated to be 51.32 N with a sample standard deviation of 13.73 N.

6.5.3 Interpretation of Borehole Simulation Results

When an additional spatial constraint in the form of a pipe is introduced to simulate the borehole during deployment, the system with the baffle reaches a constant terminal velocity. This implies that the accelerating forces are equal to the decelerating forces. Furthermore, it becomes evident that the drag of the baffle is significantly greater in this case, as the same accelerating mass does not produce any acceleration in this scenario.

The increased drag of the baffle in the presence of the pipe can be explained by several factors.

Firstly, the pipe constrains the space available for water to flow around the baffle, leading to increased interaction between the water and the baffle. This heightened interaction directly contributes to the increased drag force on the baffle.

Additionally, there is an increase in dynamic pressure within the pipe. The baffle partially blocks and redirects the flow of water, which leads to a buildup of pressure as the water is forced to flow around it. This pressure generates a force that opposes the motion of the baffle, further adding to the resistance and making it more difficult for the system to accelerate. Without the pipe, the water would have more freedom to move and the pressure buildup would be lower, but within the pipe, this focused flow significantly increases the drag experienced by the baffle.

These factors collectively explain why the drag force on the baffle is significantly larger when the pipe is introduced, leading to a situation where the same accelerating mass is unable to produce any acceleration.

Since the terminal velocity is reached in this scenario and the calculated drag corresponds precisely to this velocity, we can now verify if the drag force indeed follows the v^2

dependency. To investigate this relationship, the following formula is used:

$$F_{\text{d, new}} = F_{\text{d, old}} \cdot \left(\frac{v_{\text{new}}}{v_{\text{old}}} \right)^2 \tag{12}$$

Assuming $F_{\text{d, old}} = 12.66$ N and $v_{\text{old}} = 0.167$ m/s and extrapolating this for a velocity of 0.3 m/s under the assumption that drag depends on the square of the velocity, we obtain 40.85 N. This result is within one standard deviation of the measured mean value of 51.32 N. This suggests that the result is consistent with the v^2 dependency, considering the variability in the measurements.

7 Conclusion and Outlook

The primary goal of this thesis was to determine the drag of the LOMlogger baffle. This was analyzed by examining the behavior of the baffle using a specially designed pulley system setup in both an open water tank and a simulated borehole environment.

The experiments revealed that the acceleration in all cases was significantly higher without the baffle, indicating the presence of additional drag introduced by the baffle. In the pipe scenario, which is simulating a realistic deployment condition, the experiments showed a significant reduction in acceleration due to the increased resistance within the confined environment, primarily caused by the restricted water flow around the baffle and the increased dynamic pressure within the pipe.

The drag of the baffle was greater in the confined environment, essentially leading the system to reach its terminal velocity. Consequently, it was determined that the drag of the baffle for a realistic deployment scenario at a lowering speed of 0.17 m/s is approximately 13 N and for a speed of 0.3 m/s, the drag was around 51 N.

These results also verified that the drag indeed depends on the square of the velocity. Through this verification, the drag can be calculated for the final lowering speed chosen for the deployment.

An important next step is to include an uncertainty analysis, particularly because this thesis did not account for the errors in the spline fits, upon which the derivatives and consequently the analysis relied on. Furthermore, video footage of the baffle during the lowering in the pipe would help analyze baffle behavior, especially near the walls. Additionally, the effects of using two baffle layers on the drag of the system could be analyzed. Last but not least, exploring different baffle-to-pipe diameter ratios would help find the optimal configuration for minimizing drag in various deployment scenarios.

Acronyms

AGN Active Galactic Nuclei. 3

CC Charged Current. 3, 6

CFD Computational Fluid Dynamics. 15

CRs Cosmic Rays. 2

DOMs Digital Optical Modules. 5, 6, 8, 10, 12

EHWD Enhanced Hot Water Drill. 12

GRBs Gamma Ray Bursts. 3

ICL IceCube Laboratory. 5, 6

ISM Interstellar Medium. 2

LOM Long Optical Module. 8, 10

NC Neutral Current. 3, 6

PMT Photo Multiplier Tube. 5, 9

POCAM Precision Optical Calibration Module. 11

RPM Revolutions Per Minute. 18

SNRs Supernova Remnants. 3

A Appendix

A.1 ***Plots for Open Water Tank without Pipe***

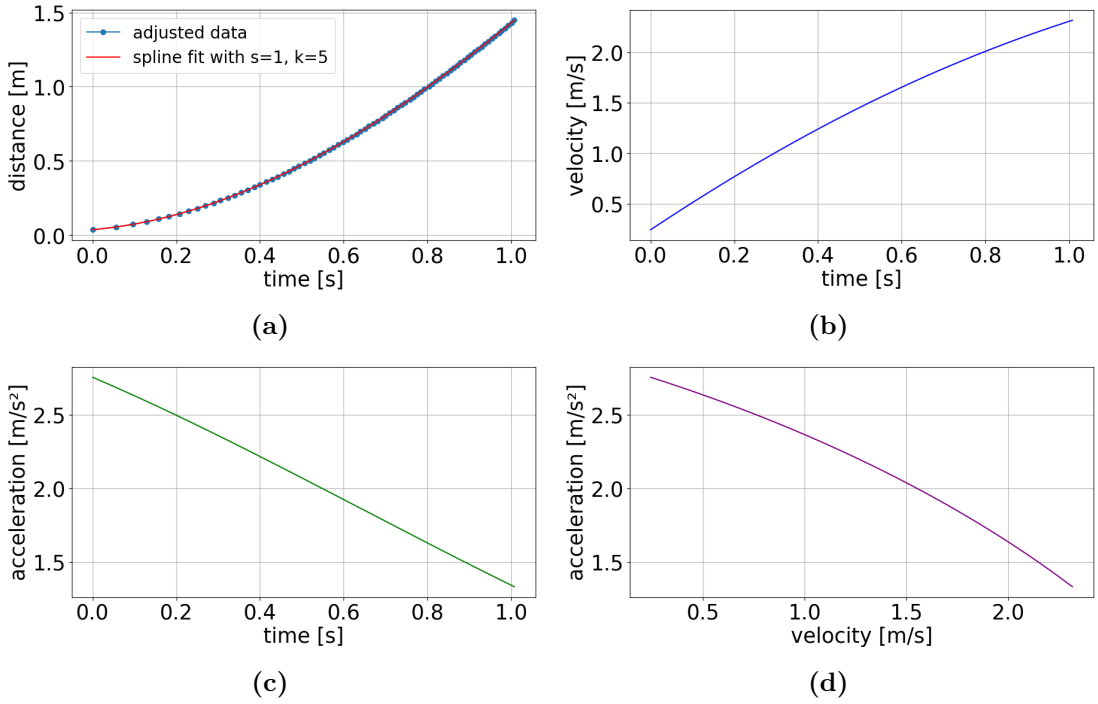

Figure 24: Reference measurements for the open water tank for the first 2500g measurement.

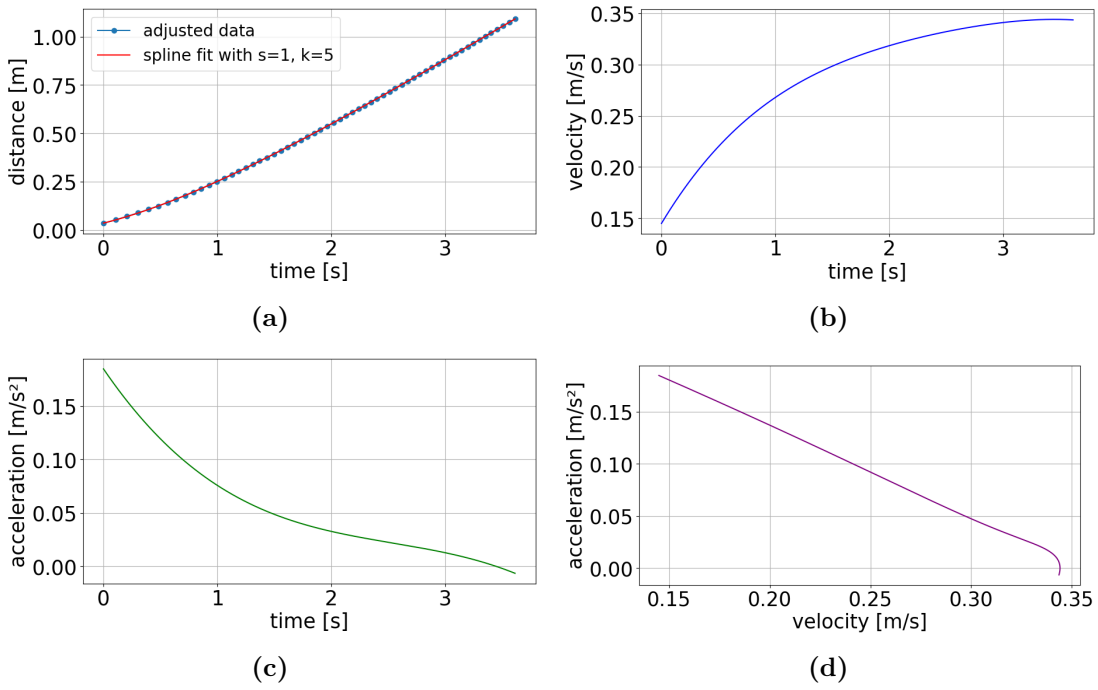

Figure 25: Measurements with the baffle for the open water tank for the first 2500g measurement.

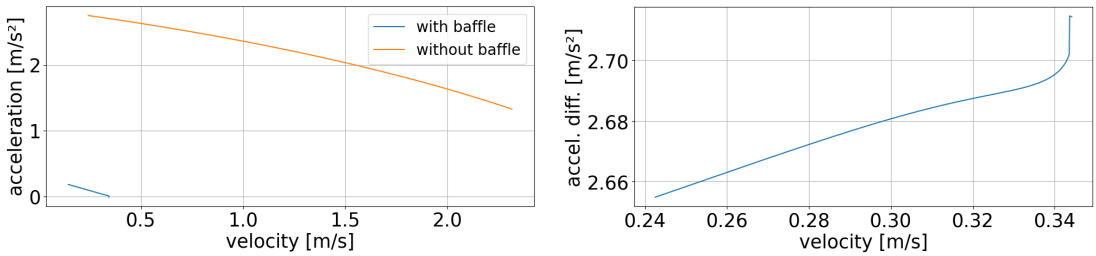

(a) **(b)**

Figure 26: Analysis of the acceleration difference for the first 2500g measurement without the pipe.

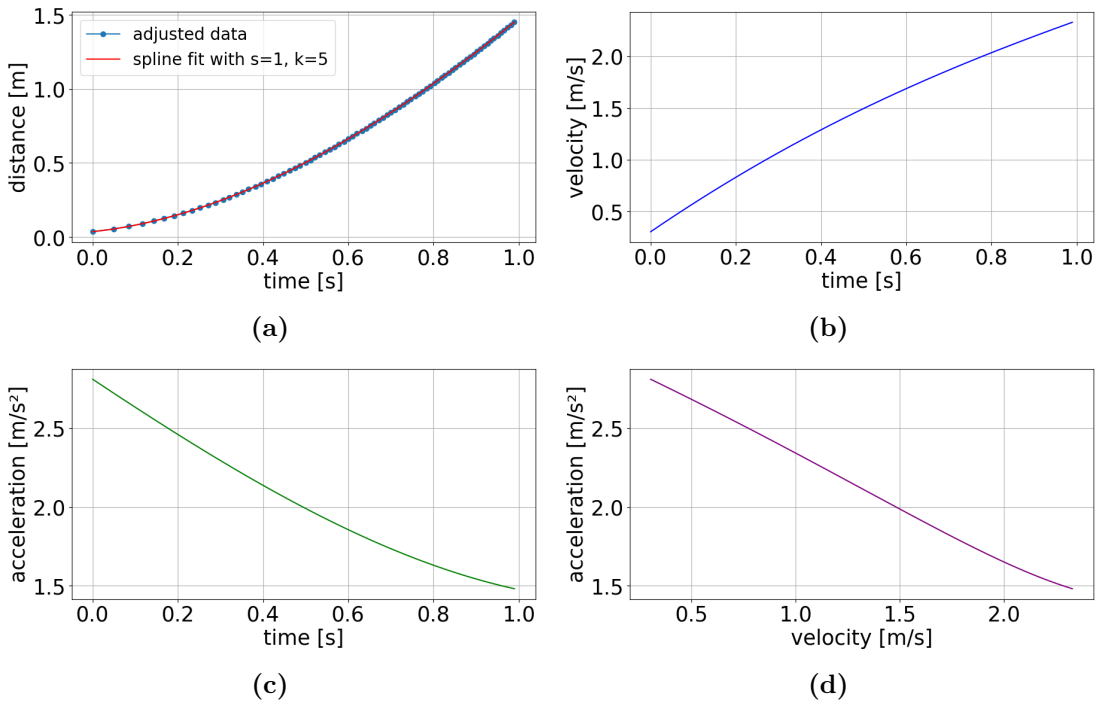

(a) (b) (c) (d)

Figure 27: Reference measurements for the open water tank for the second 2500g measurement.

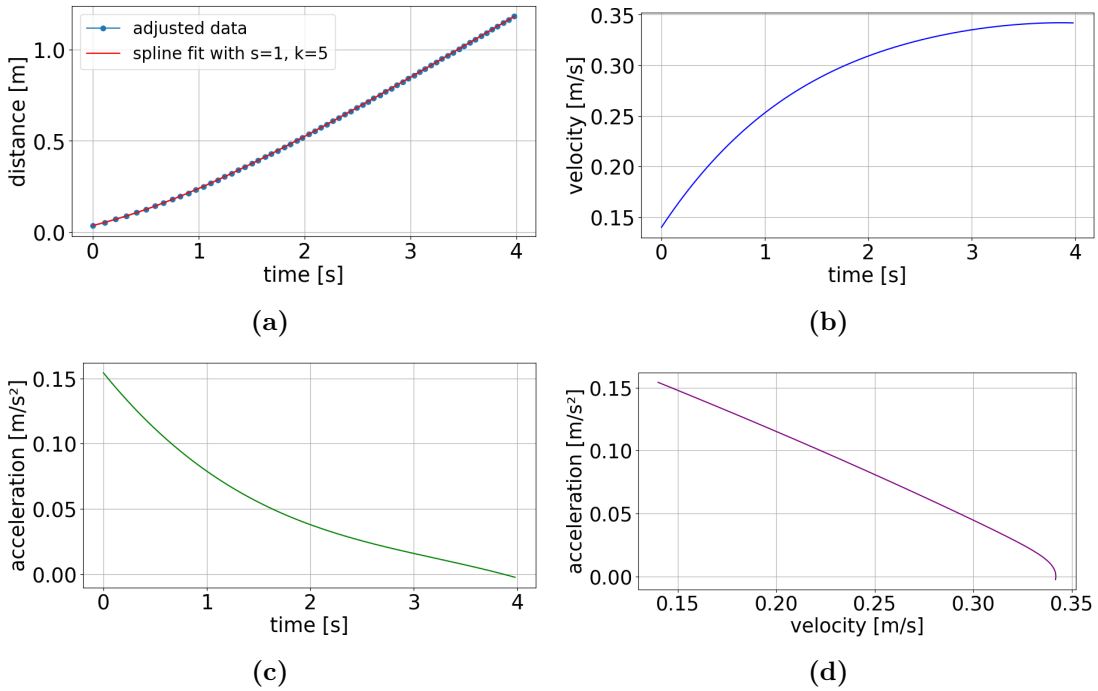

(a) (b) (c) (d)

Figure 28: Measurements with the baffle for the open water tank for the second 2500g measurement.

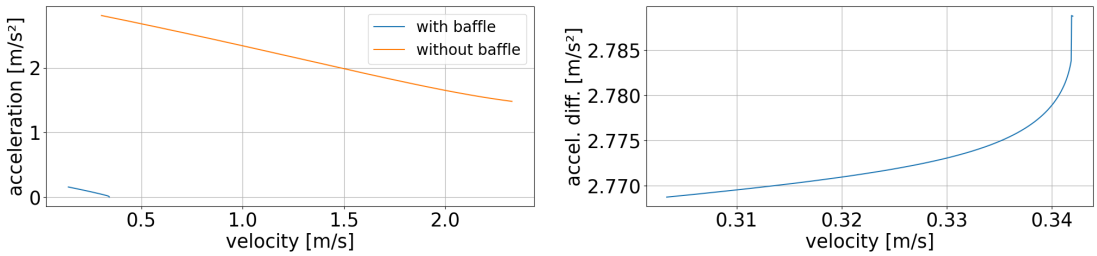

(a) **(b)**

Figure 29: Analysis of the acceleration difference for the second 2500g measurement without the pipe.

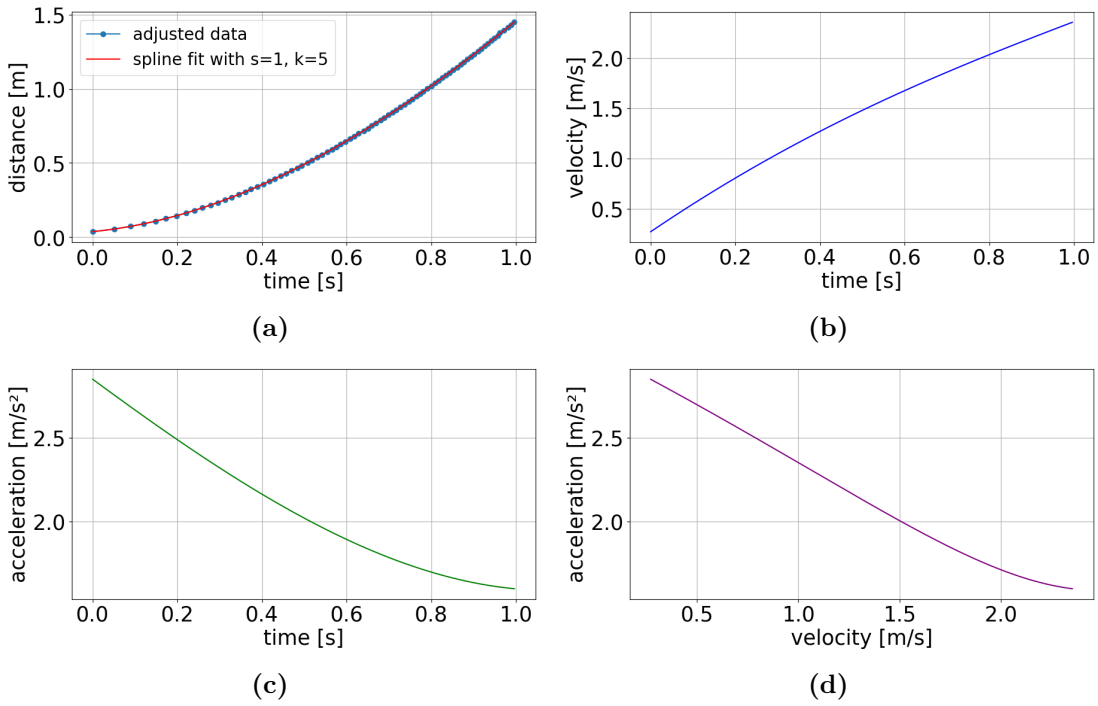

Figure 30: Reference measurements for the open water tank for the third 2500g measurement.

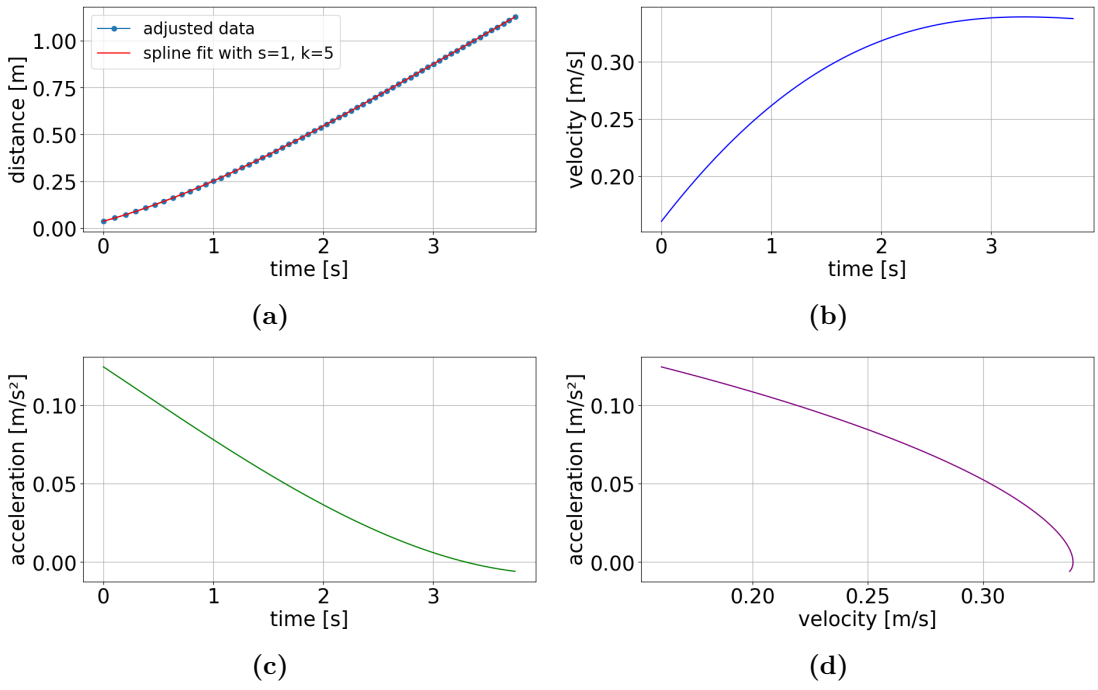

Figure 31: Measurements with the baffle for the open water tank for the third 2500g measurement.

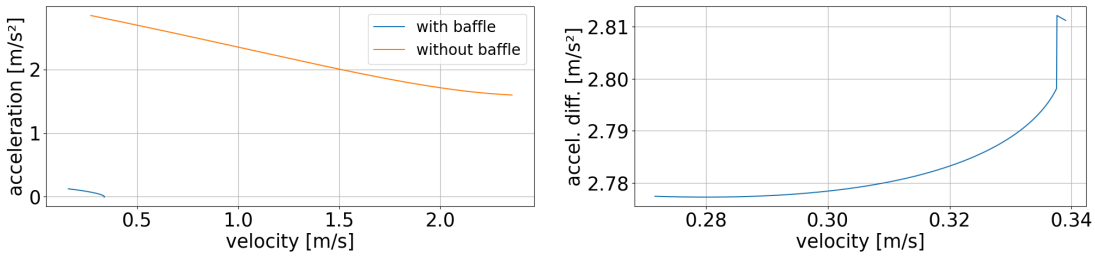

(a) **(b)**

Figure 32: Analysis of the acceleration difference for the third 2500g measurement without the pipe.

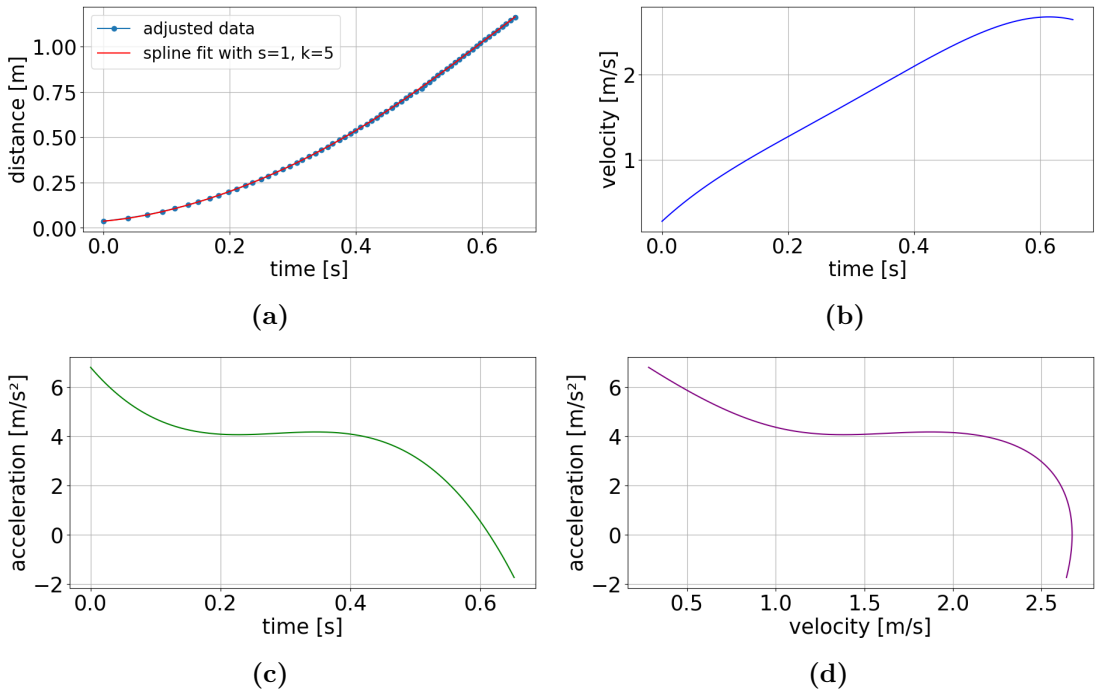

Figure 33: Reference measurements for the open water tank for the first 4500g measurement.

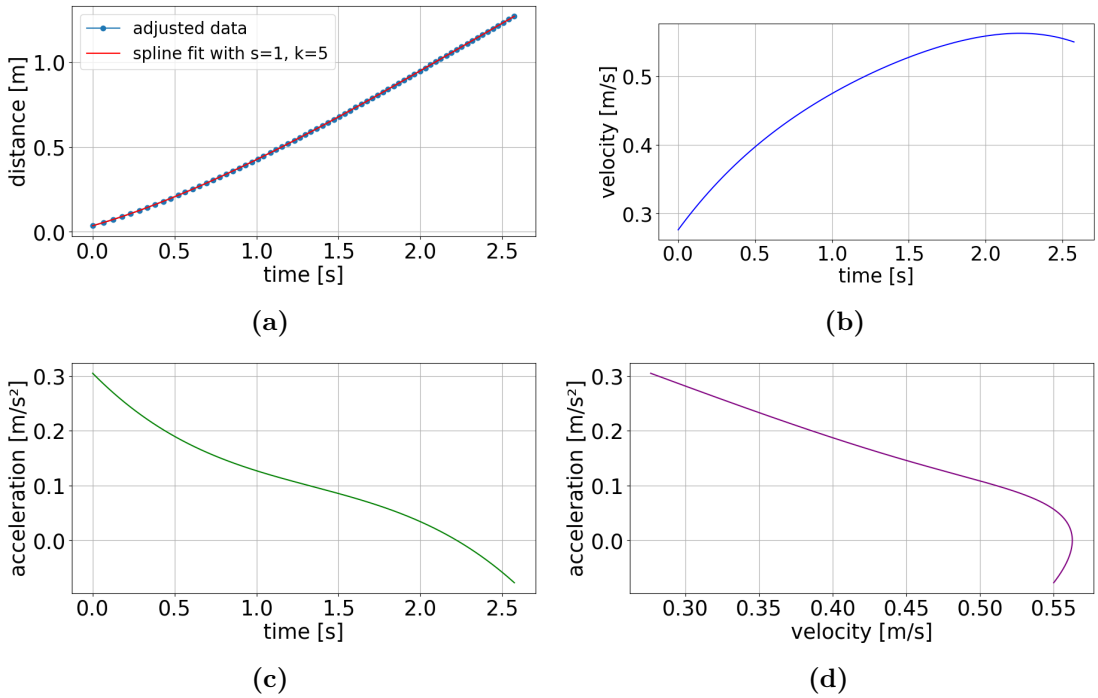

Figure 34: Measurements with the baffle for the open water tank for the first 4500g measurement.

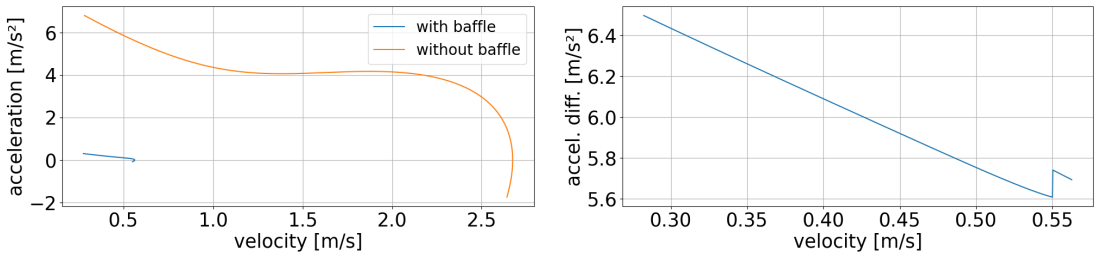

(a) **(b)**

Figure 35: Analysis of the acceleration difference for the first 4500g measurement without the pipe.

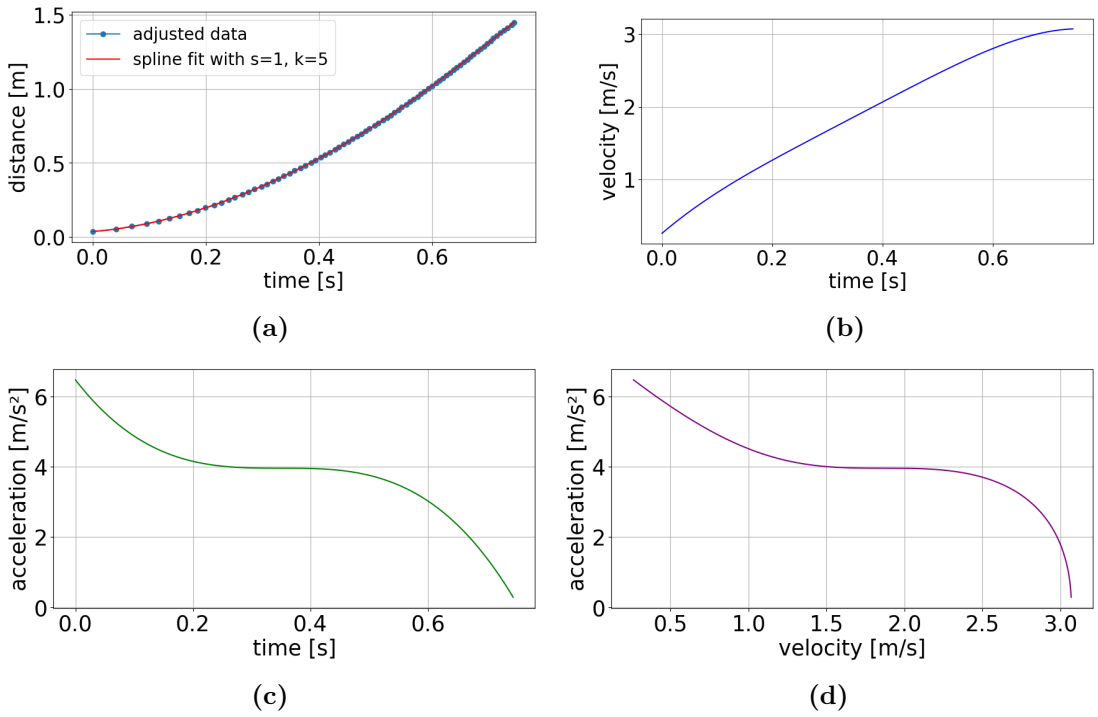

(a) (b) (c) (d)

Figure 36: Reference measurements for the open water tank for the second 4500g measurement.

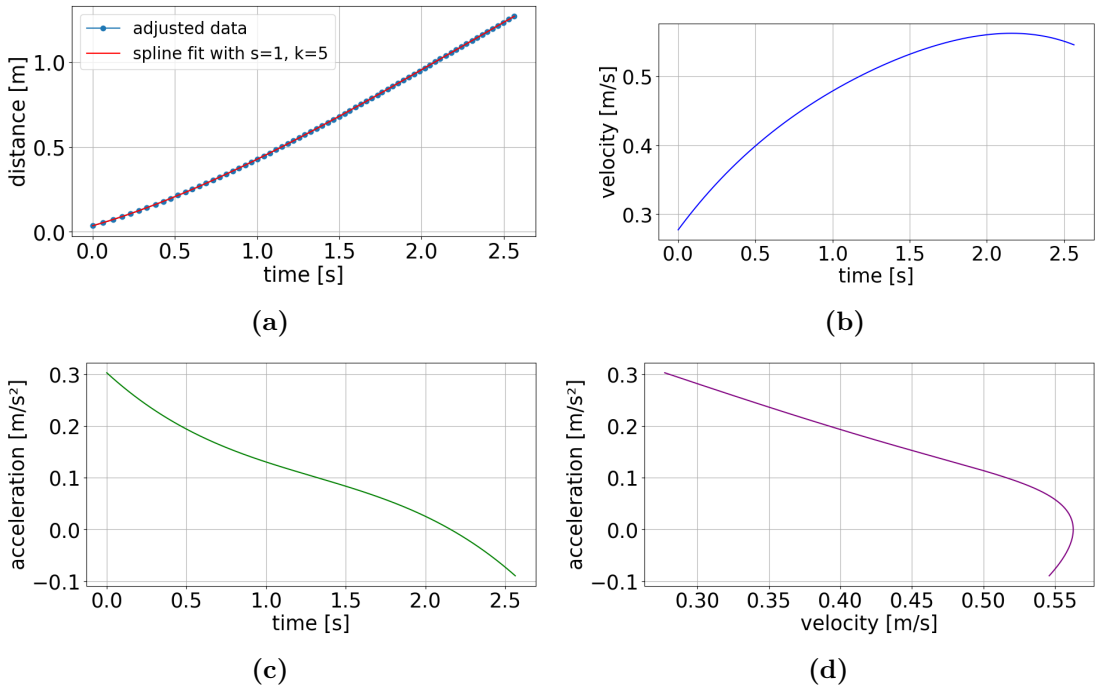

(a) (b) (c) (d)

Figure 37: Measurements with the baffle for the open water tank for the second 4500g measurement.

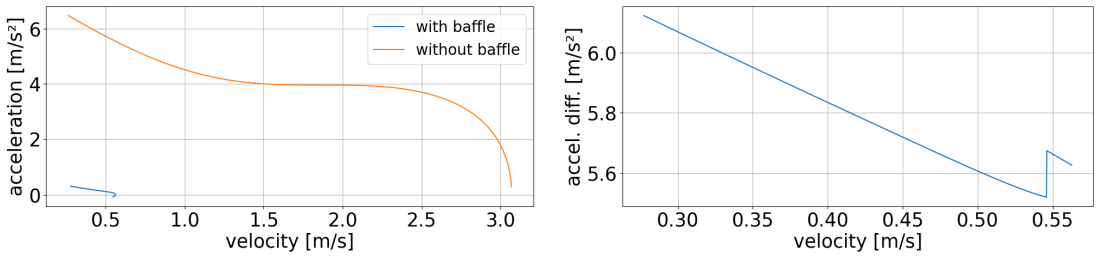

(a) **(b)**

Figure 38: Analysis of the acceleration difference for the second 4500g measurement without the pipe.

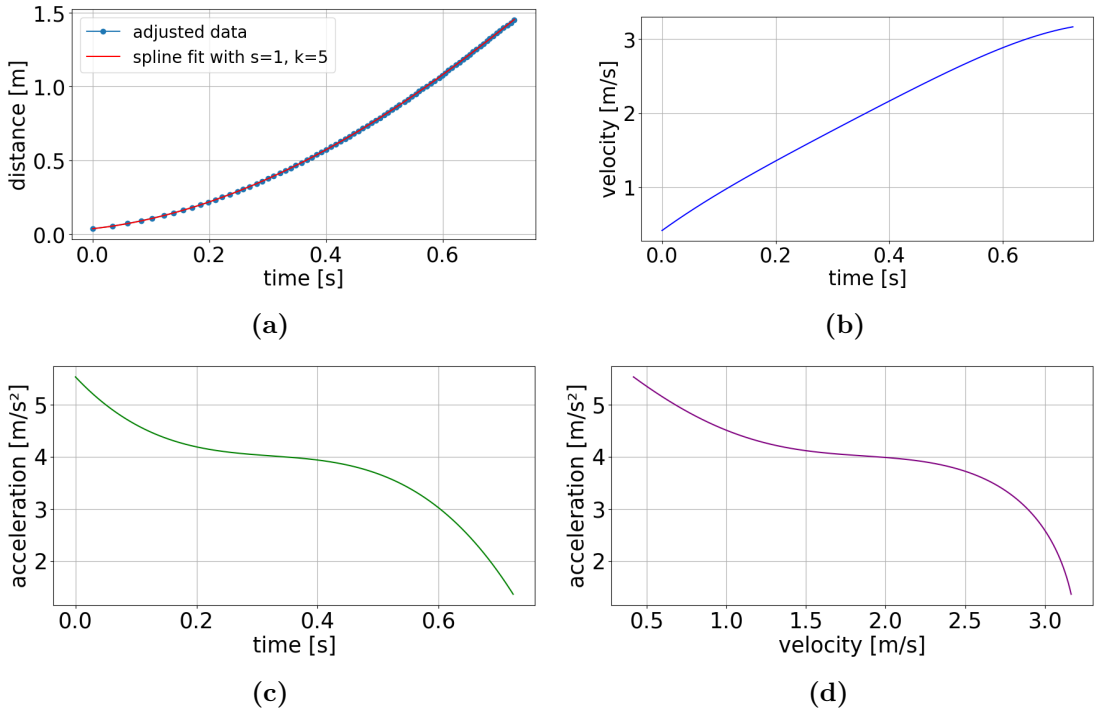

(a) (b) (c) (d)

Figure 39: Reference measurements for the open water tank for the third 4500g measurement.

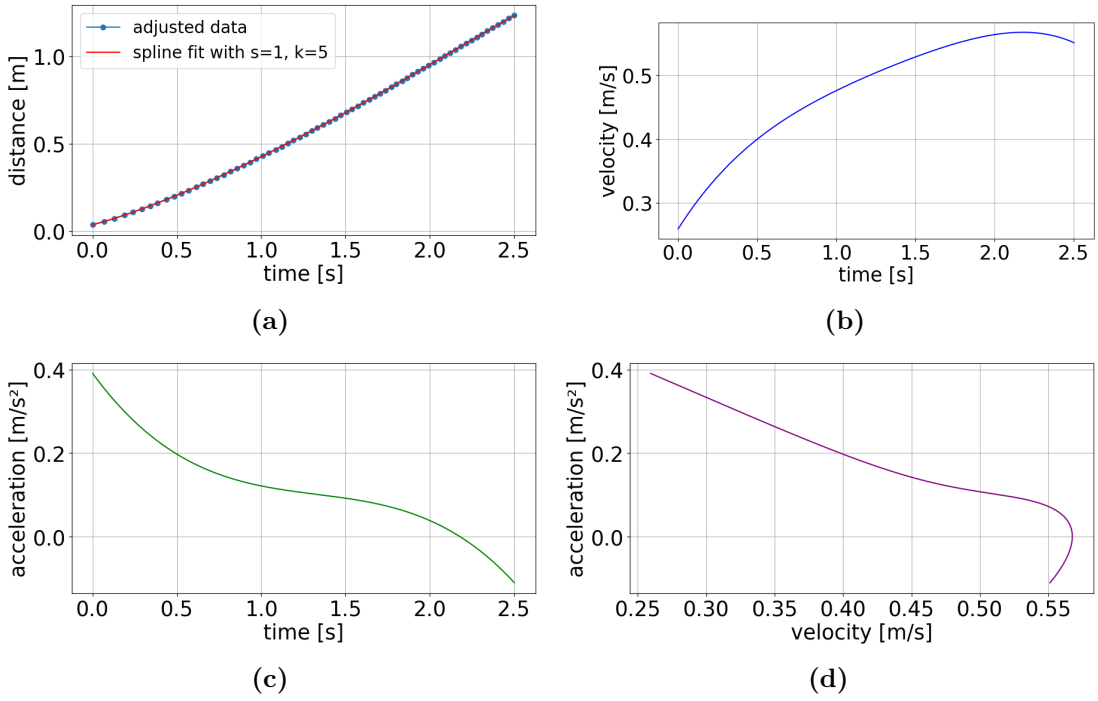

(a) (b) (c) (d)

Figure 40: Measurements with the baffle for the open water tank for the third 4500g measurement.

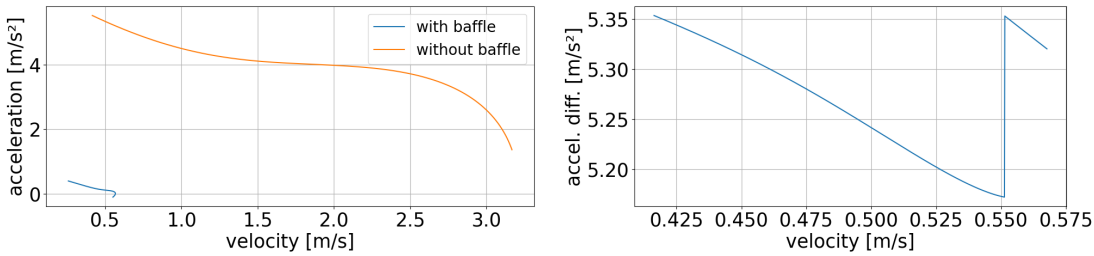

(a) **(b)**

Figure 41: Analysis of the acceleration difference for the third 4500g measurement without the pipe.

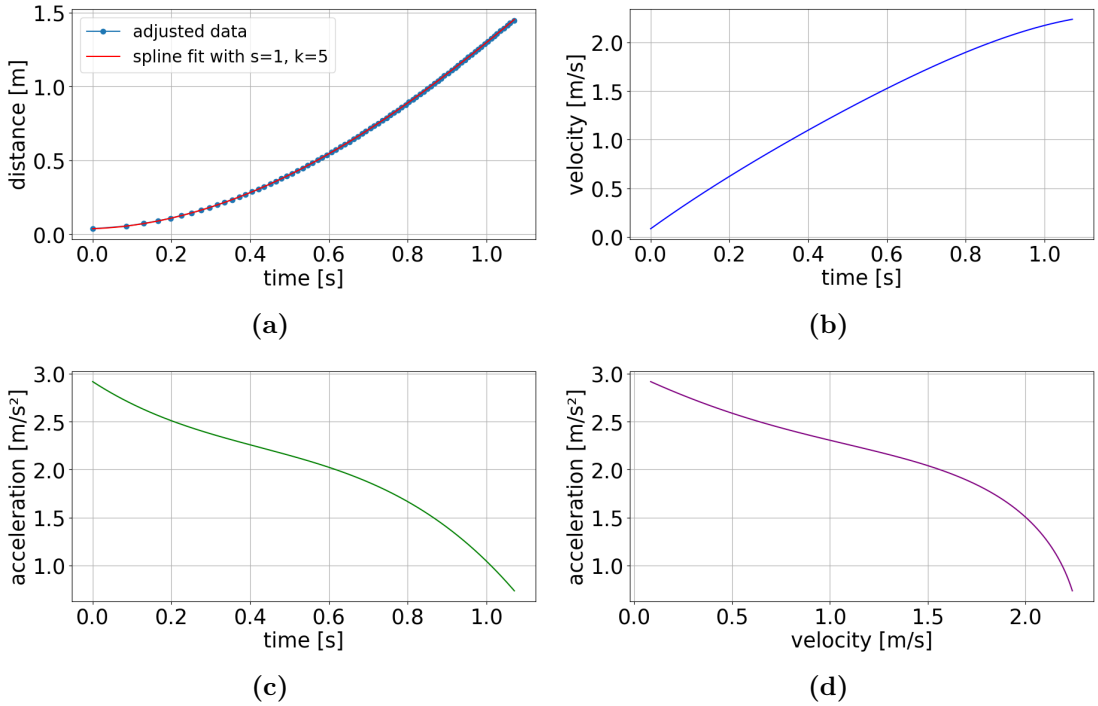

Figure 42: Reference measurements for the simulated borehole scenario for the first 2500g measurement.

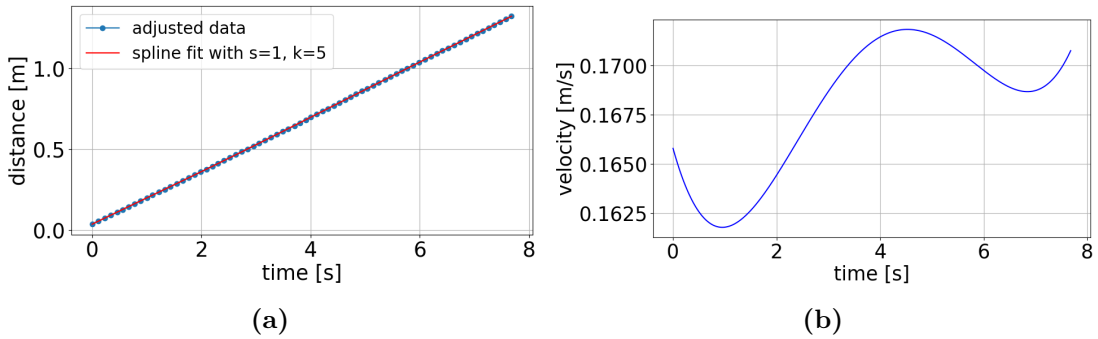

Figure 43: Measurements with the baffle for the simulated borehole scenario for the first 2500g measurement.

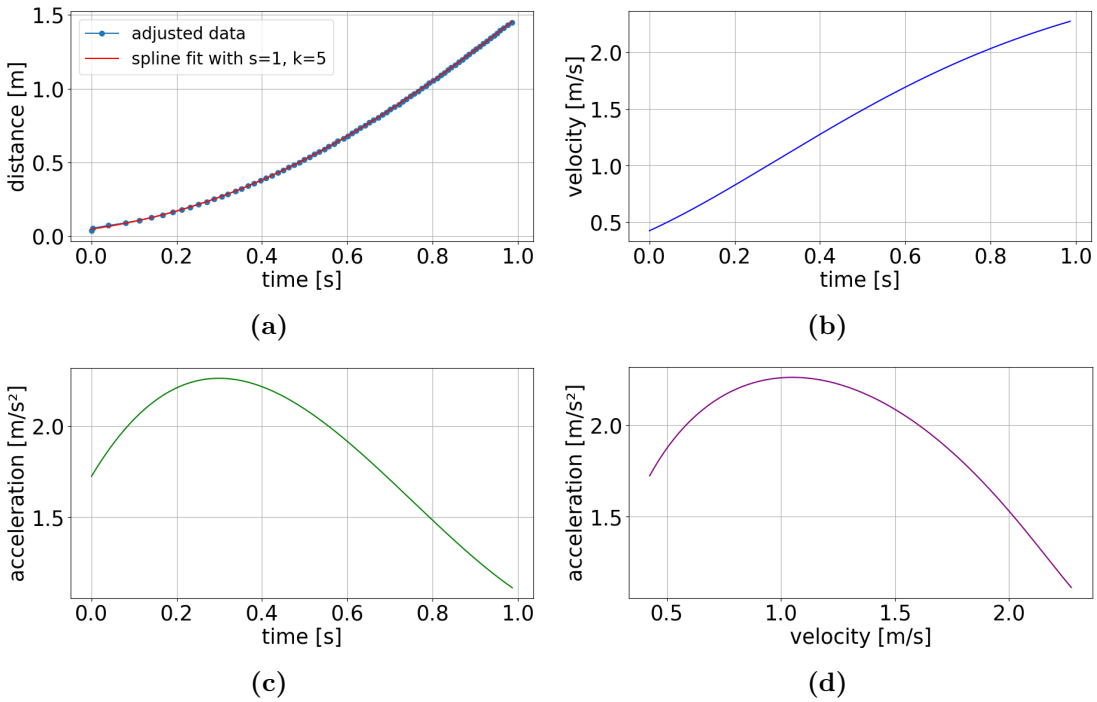

Figure 44: Reference measurements for the simulated borehole scenario for the second 2500g measurement without baffle.

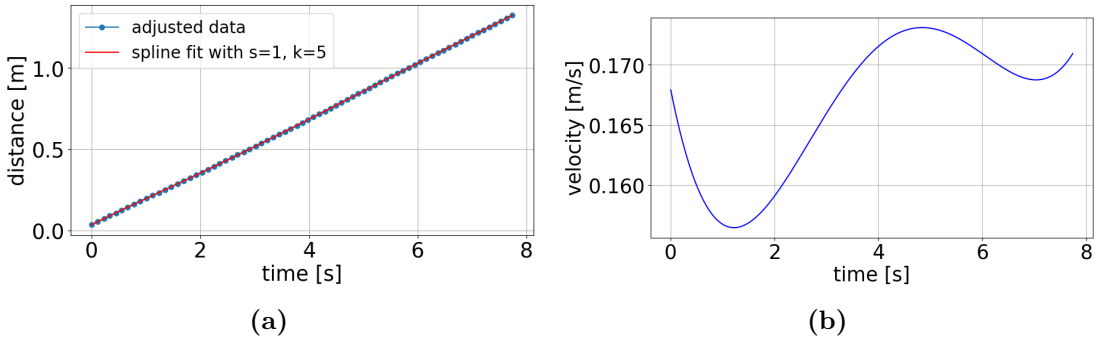

Figure 45: Measurements with the baffle for the simulated borehole scenario for the second 2500g measurement.

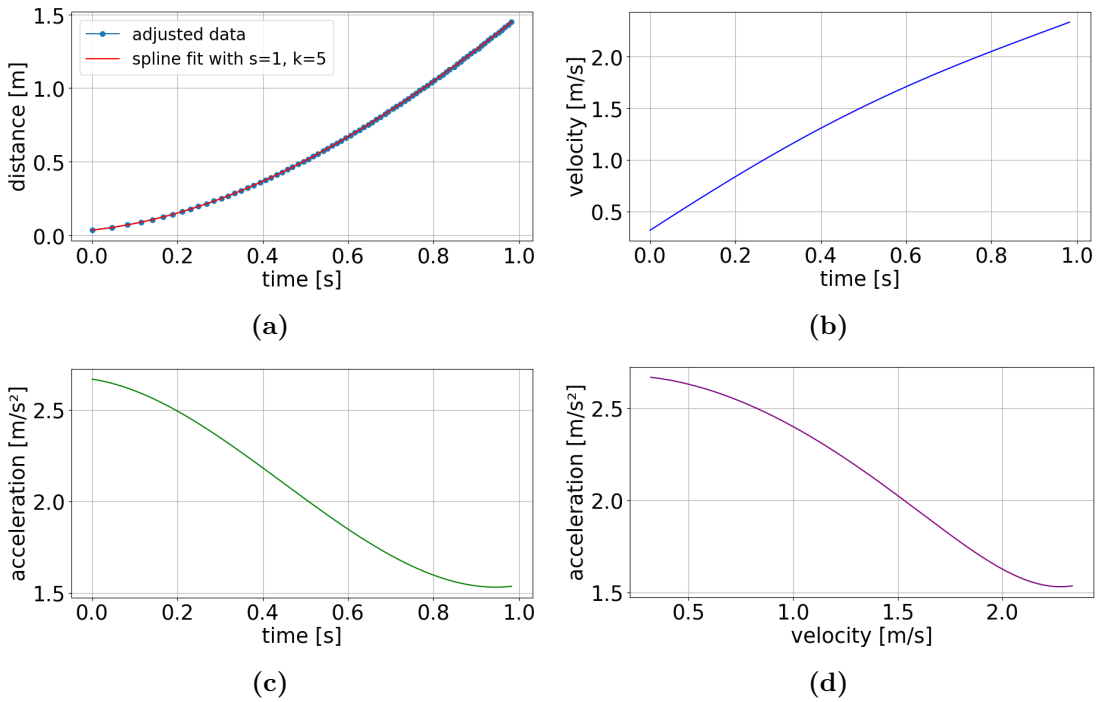

Figure 46: Reference measurements for the simulated borehole scenario for the third 2500g measurement without baffle.

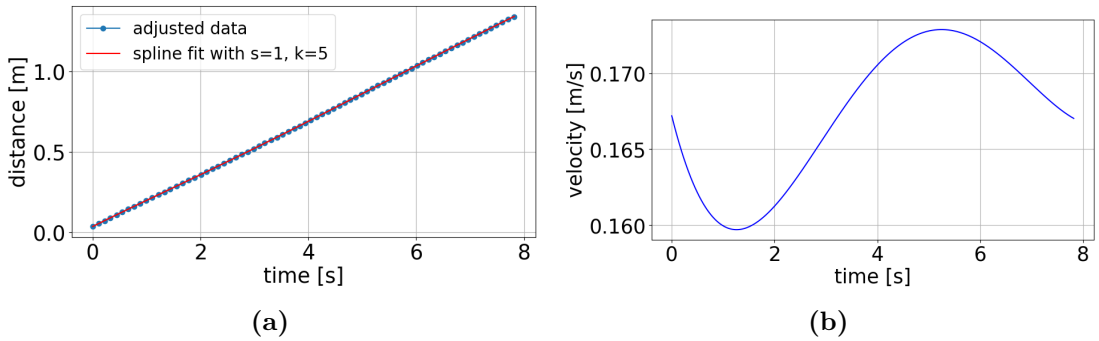

Figure 47: Measurements with the baffle for the simulated borehole scenario for the third 2500g measurement.

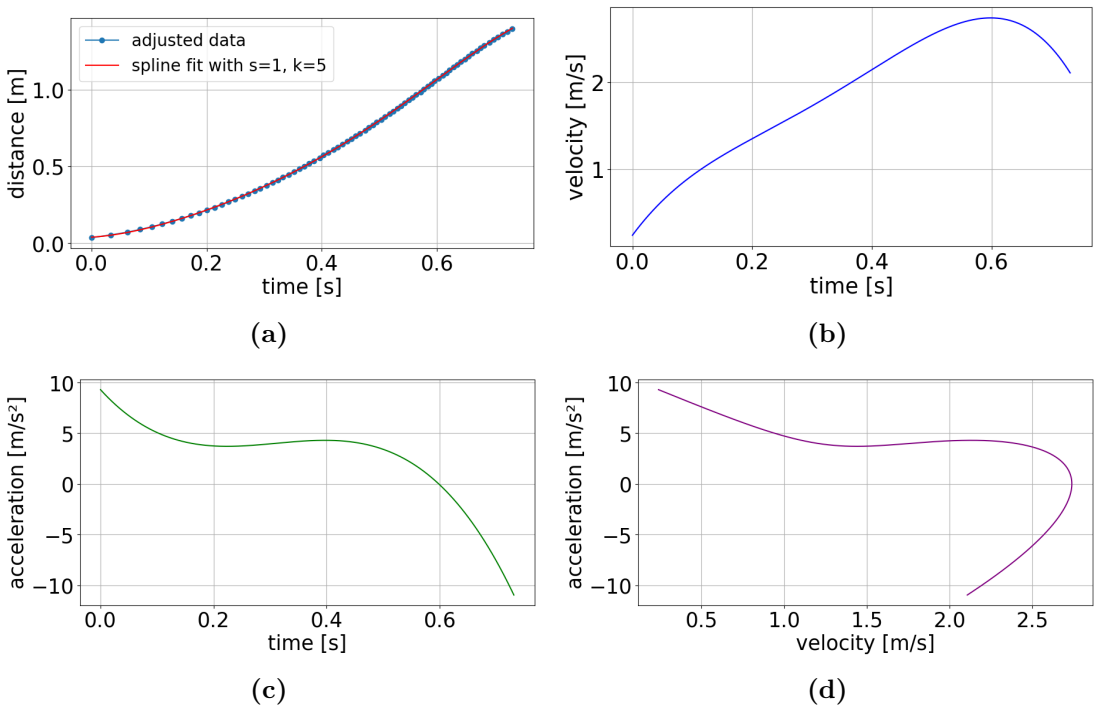

Figure 48: Reference measurements for the simulated borehole scenario for the first 4500g measurement without baffle.

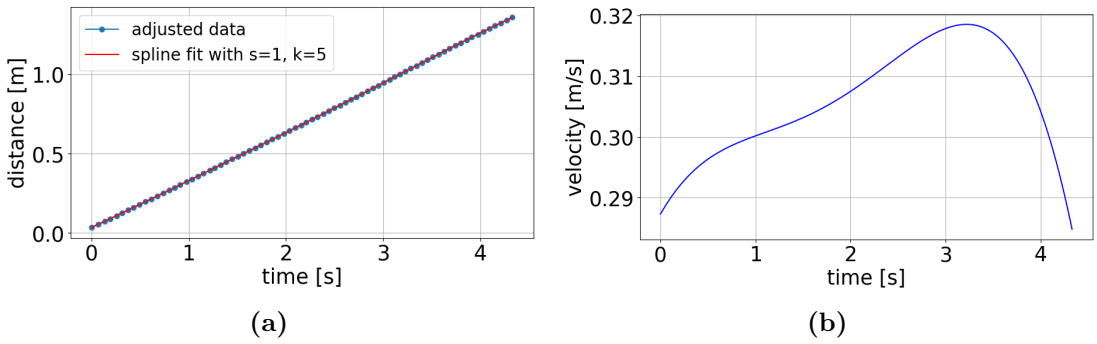

Figure 49: Measurements with the baffle for the simulated borehole scenario for the first 4500g measurement.

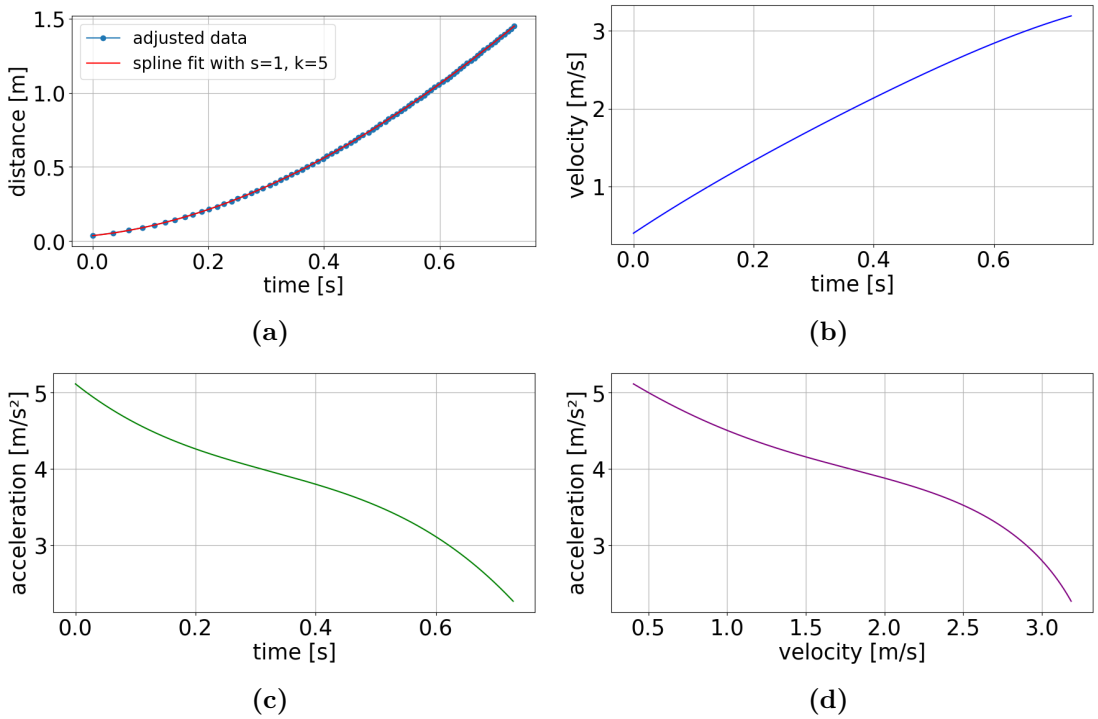

Figure 50: Reference measurements for the simulated borehole scenario for the second 4500g measurement without baffle.

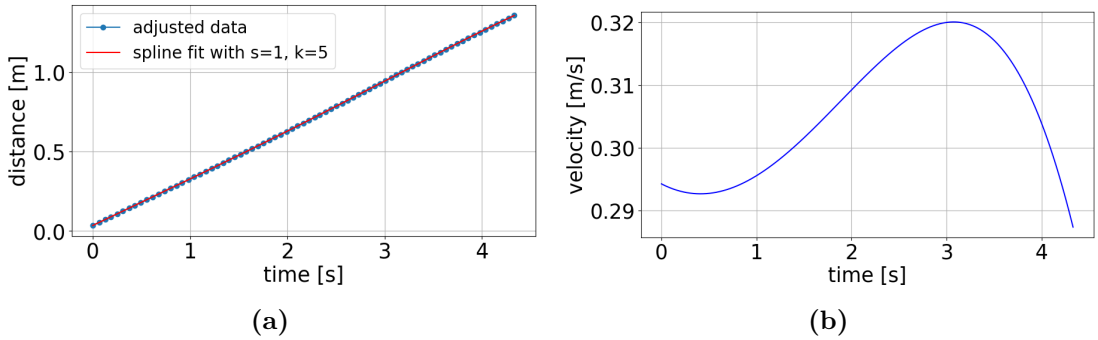

Figure 51: Measurements with the baffle for the simulated borehole scenario for the second 4500g measurement.

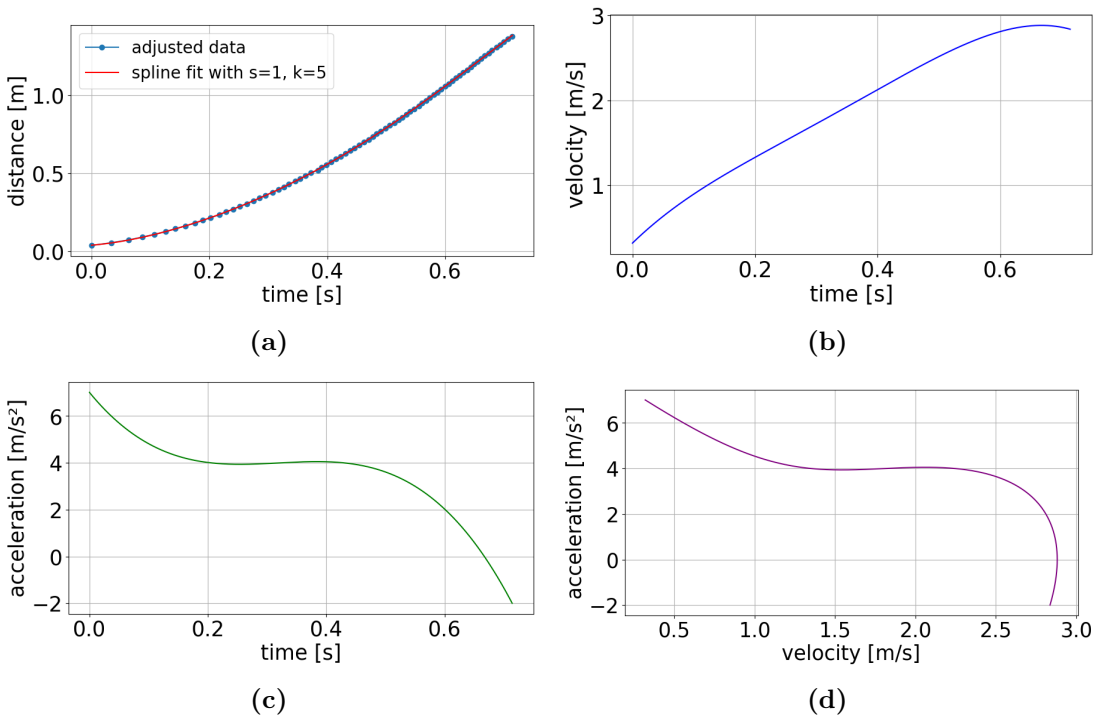

(a) (b) (c) (d)

Figure 52: Reference measurements for the simulated borehole scenario for the third 4500g measurement without baffle.

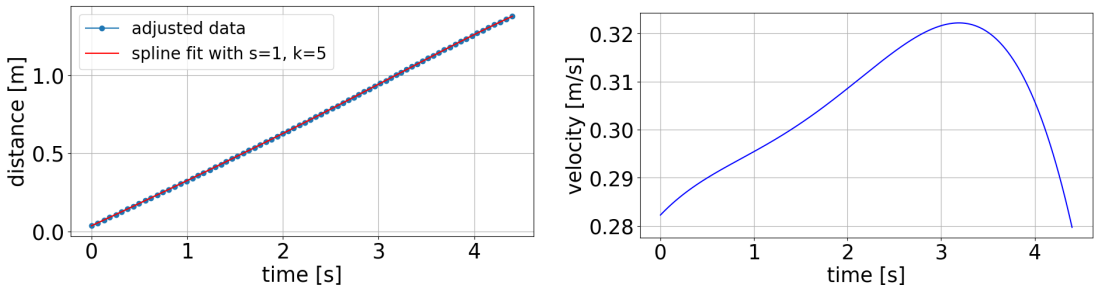

(a) (b)

Figure 53: Measurements with the baffle for the simulated borehole scenario for the third 4500g measurement.

Bibliography

[1] Zhizhong Xing and Shun Zhou. *Neutrinos in Particle Physics, Astronomy and Cosmology*. Advanced Topics in Science and Technology in China. Berlin, Heidelberg: Springer, 2011. ISBN: 978-3-642-17560-2. DOI: 10.1007/978-3-642-17560-2. URL: https://link.springer.com/book/10.1007/978-3-642-17560-2.

[2] W. Pauli. „Dear radioactive ladies and gentlemen“. In: *Phys. Today* 31N9 (1978), p. 27.

[3] C. L. Cowan, F. Reines, F. B. Harrison, H. W. Kruse, and A. D. McGuire. „Detection of the free neutrino: A Confirmation“. In: *Science* 124 (1956), pp. 103–104. DOI: 10.1126/science.124.3212.103.

[4] IceCube Collaboration. *A first look at how the Earth stops high-energy neutrinos in their tracks*. Accessed: 2024-07-25. 2017. URL: https://icecube.wisc.edu/news/press-releases/2017/11/first-look-at-how-earth-stops-high-energy-neutrinos-in-their-tracks/.

[5] Maurizio Spurio. *Probes of Multimessenger Astrophysics: Charged Cosmic Rays, Neutrinos, γ-Rays and Gravitational Waves*. Second Edition. Astronomy and Astrophysics Library. Springer, 2021. ISBN: 978-3-030-75917-8. URL: https://www.springer.com/gp/book/9783030759161.

[6] Francis Halzen and Spencer R. Klein. „Invited Review Article: IceCube: An instrument for neutrino astronomy“. In: *Review of Scientific Instruments* 81.8 (Aug. 2010). ISSN: 1089-7623. DOI: 10.1063/1.3480478. URL: http://dx.doi.org/10.1063/1.3480478.

[7] R. Abbasi, M. Ackermann, J. Adams, J. A. Aguilar, et al. „Observation of high-energy neutrinos from the Galactic plane“. In: *Science* 380.6652 (June 2023), 1338–1343. ISSN: 1095-9203. DOI: 10.1126/science.adc9818. URL: http://dx.doi.org/10.1126/science.adc9818.

[8] Aya Ishihara. *The IceCube Upgrade – Design and Science Goals*. 2019. arXiv: 1908.09441 [astro-ph.HE]. URL: https://arxiv.org/abs/1908.09441.

[9] M. Aartsen, Rezvan Abbasi, Yasser Abdou, M. Ackermann, et al. „South Pole Glacial Climate Reconstruction from Multi-Borehole Laser Particulate Stratigraphy“. In: *Journal of Glaciology* 59 (Sept. 2013), pp. 1117–1129. DOI: 10.3189/2013JoG13J068.

[10] M.G. Aartsen et al. „The IceCube Neutrino Observatory: Instrumentation and Online Systems“. In: *Journal of Instrumentation* arXiv:1612.05093 [astro-ph.IM] (Dec. 2016). DOI: 10.1088/1748-0221/12/03/P03012.

[11] Thomas K. Gaisser, Ralph Engel, and Elisa Resconi. „Cosmic Rays and Particle Physics“. In: Cambridge University Press, 2016.

[12] U.F. Katz and Ch. Spiering. „High-energy neutrino astrophysics: Status and perspectives“. In: *Progress in Particle and Nuclear Physics* 67.3 (July 2012), 651–704. ISSN: 0146-6410. DOI: 10.1016/j.ppnp.2011.12.001. URL: http://dx.doi.org/10.1016/j.ppnp.2011.12.001.

[13] M.G. Aartsen et al. „Energy reconstruction methods in the IceCube neutrino telescope“. In: *Journal of Instrumentation* 9.03 (Mar. 2014), P03009–P03009. ISSN: 1748-0221. DOI: 10.1088/1748-0221/9/03/p03009. URL: http://dx.doi.org/10.1088/1748-0221/9/03/P03009.

[14] Anne Schukraft. „Search for a Diffuse Flux of Extragalactic Neutrinos with the IceCube Neutrino Observatory“. PhD thesis. RWTH Aachen University, 2013. URL: https://publications.rwth-aachen.de/record/229692/files/4689.pdf.

[15] Markus Ahlers, Klaus Helbing, and Carlos Pérez de los Heros. „Probing particle physics with IceCube“. In: *The European Physical Journal C* 78.11 (Nov. 2018). ISSN: 1434-6052. DOI: 10.1140/epjc/s10052-018-6369-9. URL: http://dx.doi.org/10.1140/epjc/s10052-018-6369-9.

[16] M. Ackermann, J. Ahrens, X. Bai, M. Bartelt, et al. „Optical properties of deep glacial ice at the South Pole“. In: *Journal of Geophysical Research: Atmospheres* 111.D13 (2006). DOI: https://doi.org/10.1029/2005JD006687. eprint: https://agupubs.onlinelibrary.wiley.com/doi/pdf/10.1029/2005JD006687. URL: https://agupubs.onlinelibrary.wiley.com/doi/abs/10.1029/2005JD006687.

[17] AntarcticGlaciers.org. *Ice Core Basics*. Royal Holloway University of London. 2024. URL: https://www.antarcticglaciers.org/glaciers-and-climate/ice-cores/ice-core-basics/.

[18] RAID collaboration. *Ground Penetrating Radar Image Showing the Stratigraphy of Bulk Ice*.

[19] Felix Ng and Edward C. King. „Kinematic waves in polar firn stratigraphy“. In: *Journal of Glaciology* 57.206 (2011), 1119–1134. DOI: 10.3189/002214311798843340.

[20] R. Abbasi, M. Ackermann, J. Adams, N. Aggarwal, et al. „In situ estimation of ice crystal properties at the South Pole using LED calibration data from the IceCube Neutrino Observatory“. In: *The Cryosphere* 18.1 (2024), pp. 75–102. DOI: 10.5194/tc-18-75-2024. URL: https://tc.copernicus.org/articles/18/75/2024/.

[21] Nobuhiro Shimizu, Aya Ishihara, and Alexander Kappes. *Performance studies for a next-generation optical sensor for IceCube-Gen2*. 2021. arXiv: 2108.05548 [astro-ph.IM]. URL: https://arxiv.org/abs/2108.05548.

[22] M G Aartsen, R Abbasi, M Ackermann, J Adams, et al. „IceCube-Gen2: the window to the extreme Universe“. In: *Journal of Physics G: Nuclear and Particle Physics* 48.6 (Apr. 2021), p. 060501. ISSN: 1361-6471. DOI: 10.1088/1361-6471/abbd48. URL: http://dx.doi.org/10.1088/1361-6471/abbd48.

[23] IceCube Collaboration. *Calibration Call*. https://drive.google.com/drive/folders/1n09kbJG9vwqUc-9fL-K_VQB-wHlZJrdR. 2024.

[24] Elisa Resconi, Martin Rongen, and Kai Krings. „The Precision Optical CAlibration Module for IceCube-Gen2: First Prototype“. In: (Aug. 2017), p. 934. DOI: 10.22323/1.301.0934.

[25] Anna Eimer. Personal Correspondence. 2024.

[26] Christopher Ng. Personal Correspondence. 2024.

[27] Bruce R. Munson, Alric P. Rothmayer, Theodore H. Okiishi, and Wade W. Huebsch. *Fundamentals of Fluid Mechanics*. 7th. Hoboken, NJ: Wiley, 2012. ISBN: 978-1118116134.

[28] Philipp Schlatter. Personal Correspondence. 2024.

[29] *TCRT5000 Sensor Datasheet*. Accessed: 2024-07-27. 2009. URL: `https://www.makershop.de/download/tcrt5000.pdf`.

Acknowledgements

This thesis would not have been possible without the invaluable assistance and encouragement of numerous people, whom I would like to thank:

- My professor, **Claudio Kopper**, for giving me the opportunity to write this thesis and contribute to the IceCube project. As a kid, I always dreamed of being part of cutting-edge science.
- My supervisor, **Martin Rongen**. Through his guidance, I have learned so many new things. His patience with my sometimes less-than-brilliant questions was especially appreciated. Despite his often busy schedule, he always found time to help me.
- **Anna Eimer**, who is currently developing the LOMlogger and was always available to assist me, even though she was heavily engaged in her own PhD work.
- **Johannes Schaefer**, who, although not officially my supervisor, helped me countless times, even on weekends. His assistance was particularly crucial during my many battles with the 3D printer. Without him, I would have lost more than a few of those battles (and perhaps my sanity).
- **Johannes Montag**, from whom I borrowed many weights and measuring instruments. Without his support, the experimental setup would not have been possible.
- **My friends, partner and everyone who proofread** various chapters of this thesis and provided constructive feedback. And of course, for enduring my endless rants about my work, my moments of desperation and everything else in between.
- **The entire ECAP team** for creating such a wonderful work environment and for the countless hours of table tennis, which provided much-needed breaks from work.
- **My family** for their endless support.

Eigenständigkeitserklärung

Hiermit versichere ich, Kübra Tekbiyik, die vorgelegte Arbeit selbstständig und ohne unzulässige Hilfe Dritter sowie ohne die Hinzuziehung nicht offengelegter und insbesondere nicht zugelassener Hilfsmittel angefertigt zu haben. Die Arbeit hat in gleicher oder ähnlicher Form noch keiner anderen Prüfungsbehörde vorgelegen und wurde auch von keiner anderen Prüfungsbehörde bereits als Teil einer Prüfung angenommen.

Die Stellen der Arbeit, die anderen Quellen im Wortlaut oder dem Sinn nach entnommen wurden, sind durch Angaben der Herkunft kenntlich gemacht. Dies gilt auch für Zeichnungen, Skizzen, bildliche Darstellungen sowie für Quellen aus dem Internet.

Mir ist insbesondere bewusst, dass die Nutzung künstlicher Intelligenz verboten ist, sofern diese nicht ausdrücklich als Hilfsmittel von dem Prüfungsleiter bzw. der Prüfungsleiterin zugelassen wurde. Dies gilt insbesondere für Chatbots (insbesondere ChatGPT) bzw. allgemein solche Programme, die anstelle meiner Person die Aufgabenstellung der Prüfung bzw. Teile derselben bearbeiten könnten.

Ort, Datum	Unterschrift